Atmos. Chem. Phys., 14, 1185–1204, 2014
www.atmos-chem-phys.net/14/1185/2014/
doi:10.5194/acp-14-1185-2014


Atmospheric Chemistry and Physics Open Access

# Vertically resolved aerosol properties by multi-wavelength lidar measurements

**M. R. Perrone**[1], **F. De Tomasi**[1], **and G. P. Gobbi**[2]

[1]Department of Mathematics and Physics, Universita' del Salento, 73100 Lecce, Italy
[2]Institute of Atmospheric Sciences and Climate, CNR, Rome, Italy

*Correspondence to:* M. R. Perrone (perrone@le.infn.it)

Received: 30 May 2013 – Published in Atmos. Chem. Phys. Discuss.: 10 July 2013
Revised: 7 December 2013 – Accepted: 18 December 2013 – Published: 3 February 2014

**Abstract.** An approach based on the graphical method of Gobbi and co-authors (2007) is introduced to estimate the dependence on altitude of the aerosol fine mode radius ($R_f$) and of the fine mode contribution ($\eta$) to the aerosol optical thickness (AOT) from three-wavelength lidar measurements. The graphical method of Gobbi and co-authors (2007) was applied to AERONET (AErosol RObotic NETwork) spectral extinction observations and relies on the combined analysis of the Ångstrom exponent ($å$) and its spectral curvature $\Delta å$. Lidar measurements at 355, 532 and 1064 nm were used in this study to retrieve the vertical profiles of $å$ and $\Delta å$ and to estimate the dependence on altitude of $R_f$ and $\eta$(532 nm) from the $å$–$\Delta å$ combined analysis. Lidar measurements were performed at the Department of Mathematics and Physics of the Universita' del Salento, in south-eastern Italy. Aerosol from continental Europe, the Atlantic, northern Africa, and the Mediterranean Sea are often advected over south-eastern Italy and as a consequence, mixed advection patterns leading to aerosol properties varying with altitude are dominant. The proposed approach was applied to ten measurement days to demonstrate its feasibility in different aerosol load conditions. The selected days were characterized by AOTs spanning the 0.26–0.67, 0.15–0.39, and 0.04–0.27 range at 355, 532, and 1064 nm, respectively. Mean lidar ratios varied within the 31–83, 32–84, and 11–47 sr range at 355, 532, and 1064 nm, respectively, for the high variability of the aerosol optical and microphysical properties. $å$ values calculated from lidar extinction profiles at 355 and 1064 nm ranged between 0.1 and 2.5 with a mean value ±1 standard deviation equal to $1.3 \pm 0.7$. $\Delta å$ varied within the $-0.1$–1 range with mean value equal to $0.25 \pm 0.43$. $R_f$ and $\eta$(532 nm) values spanning the 0.05–0.3 µm and the 0.3–0.99 range, respectively, were associated with the $å$–$\Delta å$ data points. $R_f$ and $\eta$ values showed no dependence on the altitude. 60 % of the data points were in the $\Delta å$–$å$ space delimited by the $\eta$ and $R_f$ curves varying within 0.80–0.99 and 0.05–0.15 µm, respectively, for the dominance of fine-mode particles in driving the AOT over south-eastern Italy. Vertical profiles of the linear particle depolarization ratio retrieved from lidar measurements, aerosol products from AERONET sun photometer measurements collocated in space and time, analytical back trajectories, satellite true colour images, and dust concentrations from the BSC–DREAM (Barcelona Super Computing Center-Dust REgional Atmospheric Model) model were used to demonstrate the robustness of the proposed method.

## 1 Introduction

Atmospheric aerosols play a central role in influencing the Earth's climate by direct, indirect, and semi-direct effects. In attempts to quantify these effects, the main difficulties arise from the very high variability in time and space of the aerosol concentration and related physical, optical, and chemical properties. The sensitivity of aerosol direct radiative effects and heating rate (HR) profiles to the vertical distribution of aerosol properties was investigated in a recent paper by one of the authors (Perrone et al., 2012). Sensitivity tests indicated that the uncertainties of the aerosol size distribution and its vertical distribution had a large impact, mainly on aerosol HR vertical profiles both in the solar and the terrestrial domain.

Lidars are currently the best devices to retrieve vertical profiles of aerosol extinction ($\alpha$) and backscattering ($\beta$) coefficients. More specifically, Raman lidars based on a tripled Nd:YAG laser are able to provide $\alpha$ and $\beta$ profiles at different wavelengths. Several numerical approaches were developed in recent years to invert $\alpha$ and $\beta$ measured at multiple wavelengths to particle parameters (Kolgotin and Muller, 2008, and references therein). In the regularization approach described in Veselovskii et al. (2002) five input optical data (three backscattering and two extinction coefficients, i.e. $3\beta+2\alpha$) were needed to retrieve the particle size distribution. A numerical approach for the linear estimation of aerosol bulk properties such as particle volume, effective radius and complex refractive index from three aerosol backscattering coefficient and one extinction coefficient (i.e. $3\beta+\alpha$) was recently developed by Veselovskii et al. (2012), since it would be highly desirable to reduce the number of optical channels in some lidar experiments. Simulation studies with regard to the feasibility of using combined observations from sun photometers and lidars for microphysical characterization of aerosol particles were reported by Pahlow et al. (2006). Subsequently, a numerical tool (LIRIC, LIdar/Radiometer Inversion Code) was developed by Chaikovsky et al. (2012) to retrieve vertically resolved aerosol microphysical properties by combining backscattering coefficient measurements at three wavelengths and sun/sky radiance measurements. This activity was performed in the framework of the European project Aerosol, Clouds, and Trace gases Research InfraStructure Network (ACTRIS, http://www.actris.net/) with the main aim of integrating sun photometer measurements from AERONET (AErosol RObotic NETwork) (Holben et al., 1998) with lidar measurements from the European Aerosol Research LIdar NETwork (EARLINET, Matthias et al., 2004). More recently, the GARRLiC (Generalized Aerosol Retrieval from Radiometer and Lidar Combined data) method was proposed by Lopatin et al. (2013). Both LIRIC and GARRLiC use the AERONET retrieval and the GARRLiC approach for treating lidar data that is based on the one used in LIRIC. However, in contrast to LIRIC, in the GARRLiC method, the size intervals of the modes may overlap and the size-independent complex refractive index may be different for each aerosol mode. Gross et al. (2011) used multi-wavelength depolarization and Raman lidar measurements to characterize the optical properties of desert dust, marine aerosols, and biomass-burning aerosol and to determine the changes with the altitude of the aerosol types. Furthermore, Ansmann et al. (2012) have proposed the single-wavelength POLIPHON (POlarization LIdar PHOtometer Networking) technique for the retrieval of particle volume and mass concentration profiles for fine- and coarse-mode particles.

The Ångstrom exponent ($å$) capability to be an indicator of the dominant size of atmospheric aerosols was exploited in this study to estimate the dependence on altitude of the aerosol size distribution from lidar measurements at three wavelengths (three optical channels). The Ångstrom exponent that is calculated from the spectral dependence of the aerosol optical thickness (AOT) is commonly used as a good indicator of the dominant size of the atmospheric particles determining the AOT. Values of $å \leq 1$ indicate size distributions dominated by coarse-mode aerosols (radii $\geq 0.5$ µm) that are typically associated with dust and sea salt particles, and values of $å \geq 1.5$ indicate size distributions dominated by fine-mode aerosols (radii $< 0.5$ µm) that are usually associated with urban pollution and biomass burning particles. Schuster et al. (2006) pointed out that it was important to consider the wavelength pair used to calculate the Ångstrom exponent when making qualitative assessments about the corresponding aerosol size distribution. They found that $å$ values calculated from longer wavelength pairs (e.g. $\lambda = 670$, 870 µm) were sensitive to the fine-mode fraction of aerosols but not the fine-mode radius. Conversely, shorter wavelength pairs (e.g. $\lambda = 380$, 440 µm) were sensitive to the fine-mode effective radius but not the fine-mode fraction. However, $å$ cannot provide information on the relative contribution of coarse- and fine-mode particles if different aerosol types are present in the air column. Large fine-mode particles can have the same $å$ as mixtures of coarse-mode and small fine-mode ones (Gobbi et al., 2007). Several authors have investigated how the spectral variation of $å$ can provide further information about the aerosol size distribution (e.g. O'Neill et al., 2003; Schuster et al., 2006, and references therein). Kaufman (1993) pointed out that negative values of the differences $\Delta å = å$ (440 nm, 613 nm) – $å$(440 nm, 1003 nm) indicated the dominance of fine-mode aerosol, while positive differences indicated the effect of two separate modes with a significant coarse-mode contribution. Futhermore, O'Neill et al. (2003) demonstrated that the recognition that the aerosol particle size distribution is bimodal permits the extraction of the fine- and coarse-mode optical depth from the spectral shape of the total aerosol optical depth. An overview of the studies on the Ångstrom exponent and its curvature has been reported in Schuster et al. (2006) and Gobbi et al. (2007). A simple graphical method to visually convert $å$ and its spectral curvature ($\Delta å$) to both the fine-mode aerosol radius and the contribution of the fine-mode aerosol to the AOT was proposed by Gobbi et al. (2007). In particular, aerosols were classified in a new space defined by $\Delta å$ vs. $å$, which was invariant to changes in AOT for a given size distribution. Quality-assured direct-sun data in the 440–870 nm wavelength range retrieved from sun photometers operating within AERONET were used by Gobbi et al. (2007) to demonstrate the feasibility of the introduced classification scheme. Considering the operating wavelengths of AERONET sun photometers, $å$ was derived for the wavelength pairs of 440–870 nm, and its spectral curvature was represented by the difference $\Delta å = å$(440, 675) – $å$(675, 870). The graphical method was applied by Gobbi et al. (2007) to the analysis of yearly records at eight sites in three continents; the sites were characterized by

different levels of pollution, biomass burning and mineral dust concentrations. Results depicted the dominance of fine-mode aerosols in driving the AOT at polluted sites. Basart et al. (2009) provided an atmospheric aerosol characterization for northern Africa, the north-eastern Atlantic, the Mediterranean region, and the Middle East by applying the $\Delta\mathring{a}$ vs. $\mathring{a}$ graphical method to direct sun observations made at 39 AERONET stations.

Lidar measurements at 355, 532 and 1064 nm are used in this study to retrieve vertical profiles of $\mathring{a}$ and its spectral curvature, $\Delta\mathring{a}$, with the aim of demonstrating the feasibility of the $\Delta\mathring{a}$–$\mathring{a}$ graphical method to provide altitude-resolved estimates of the fine-mode aerosol radius and the fine-mode contribution to the AOT, when atmospheric particles from different sources; and hence of different types are present along the aerosol column. Depolarization lidar measurements, AERONET sun photometer measurements collocated in space and time with lidar measurements, satellite true colour images, analytical back trajectories, and dust concentrations from the BSC–DREAM (Barcelona Super Computing Center-Dust REgional Atmospheric Model) model (www.bsc.es) have been used to understand/support the change with altitude of the aerosol properties revealed by the graphical method. A short version of this paper was presented at the 9th International Symposium on Tropospheric Profiling (Cavalieri et al., 2012). An overview of the 3 wavelength lidar system and measurements is provided in Sect. 2. The aerosol classification framework used is discussed in Sect. 3. Subsequently, four study cases are presented and discussed in detail in Sect. 4. Results referring to 10 measurements days with different aerosol types in the air column are presented in Sect. 5. Summary and conclusion are given in Sect. 6.

## 2 Lidar system and measurements

### 2.1 Description of the lidar system

The ground-based lidar system operating at the Department of Mathematics and Physics of the Universita' del Salento (Lecce) in south-eastern Italy (40.33° N; 18.11° E) and identified as UNILE (UNIversity of LEcce) lidar was used in this study. The UNILE lidar activity has been carried out within EARLINET since May 2000. The UNILE lidar system is nowadays composed of a 30 Hz Nd:YAG laser operating at its fundamental wavelength, 1064 nm, and the second and third harmonic at 532 and 355 nm, respectively. The linear polarized laser pulses are about 10 ns long. The maximum energy per pulse is 1000 mJ, 150 mJ and 300 mJ, at 1064, 532, and 355 nm, respectively. The 3-wavelength laser beams delivered by the Nd:YAG laser which are spatially separated, are recombined in one beam by dichroic mirrors and sent in the atmosphere by means of a mirror located on the axis of a f/4 Newton telescope. The backscattered radiation collected by the primary mirror of the Newton telescope and collimated by a plano convex lens, is spectrally resolved by means of dichroic mirrors and interferential filters. Subsequently, the 1064 nm signal is detected by an avalanche photodiode and an A/D transient recorder. The signals at 532 and 355 nm are detected by photomultipliers connected to transient recorders that have both a 12 bit A/D conversion and a photon-counting (PC) capability. In this way, the full dynamic range of the lidar signals can be monitored. Transient recorders integrate over 2000 laser shots that correspond to about 60 s. The lidar system is estimated to achieve full overlap between 0.5–1.0 km above the ground level (a.g.l.).

### 2.2 Aerosol parameters from lidar measurements

The UNILE lidar system was designed to derive vertical profiles of the aerosol extinction ($\alpha(z)$) or backscattering ($\beta(z)$) coefficient at 355 nm, 532 nm and 1064 nm, respectively and of the linear volume depolarization ratio ($\delta(z)$) at 355 nm during day time measurements. The approach proposed by Fernald (1984) and Klett (1985), which requires an a priori value of the aerosol extinction-to-backscatter ratio (also referred to as the aerosol lidar ratio, LR), is commonly used to invert lidar signal profiles and extract aerosol extinction and backscattering coefficient profiles. The assumption that LR is known a priori is likely the largest source of systematic error within this lidar inversion procedure. However, this uncertainty can be largely reduced if additional information is available. Takamura et al. (1994) considered the possibility of removing the indeterminacy in LR by combining lidar data with independent measurements of the aerosol optical thickness. Then, Di Girolamo et al. (1994) and Marenco et al. (1997) suggested an alternative inversion technique, which, through an iterative procedure, allows one to determine $\alpha(z)$ and $\beta(z)$ by using as boundary conditions (1) the AOT of a selected altitude range and (2), as in the Fernald–Klett approach, the total backscattering coefficient $\beta_T$ (due to molecules ($\beta_M$) and aerosol ($\beta$) ) at a far-end reference height $z_f$. This last approach was used in this study to extract aerosol extinction profiles at 355 nm, 532 nm, and 1064 nm, from UNILE lidar measurements. AOT values at the lidar wavelengths were retrieved from AERONET sun/sky photometer measurements collocated in space and time. An AERONET sun/sky photometer has operated at the UNILE lidar site since 2003, and it provides AOTs with accuracy of $\pm 0.01$, according to Dubovik et al. (2002). Hence, it was required that the AOTs calculated from the aerosol extinction profiles should not exceed (within $\pm 0.01$) the corresponding AOT values retrieved from collocated sun/sky photometer measurements. To this end, we have assumed that $\alpha(z)$ does not vary with altitude below the height ($z_i$) where the lidar system achieves the full overlap. The full overlap height varies within 0.5–1.0 km a.g.l. for the lidar system of this study. Note that the planetary boundary layer (PBL) height on average varies within 0.4–1.0 km a.g.l. at the monitoring

site of this study (De Tomasi and Perrone, 2006; De Tomasi et al., 2011). Aerosol particles are well mixed within the PBL and, as a consequence, it is reasonable to assume that $\alpha(z)$ does not vary with altitude below $\sim 1$ km a.g.l. The far-end reference height was chosen, for each profile, in a region where the lidar signal follows the molecular profile; and hence it was assumed $\beta_T(z_f) \cong \beta_M(z_f)$. Note that the assumption of an altitude-independent lidar ratio to retrieve $\alpha(z)$ profiles was still necessary for the iterative procedure used in this study. A discussion on this assumption is reported in Sect. 4.1.1. Uncertainties in the retrieved $\alpha(z)$ profiles include statistical uncertainties due to the presence of noise on the received lidar signals as well as systematic uncertainties, i.e. those due to the assumed molecular profile, the reference backscattering coefficient value, the total measured AOT, the AOT contribution of the atmospheric layer below the overlap height $z_i$, and the lidar ratio variability. Radiosonde measurements at the meteorological station of Brindisi (http://esrl.noaa.gov/raobs/), which is 40 km northwest of the monitoring site of this study, were used to define air density vertical profiles. The uncertainty of the reference backscattering coefficient value was accounted for by assuming that the aerosol backscattering coefficient varied from a nil value up to $5 \times 10^{-7}$ $(\mathrm{m\,sr})^{-1}$ at $z = z_f$. The error on the AOT contribution of the atmospheric layer extending from the ground level up to $z_i$, which is indicated as $\mathrm{AOT}_1$, was accounted for by allowing it to increase up to 30 % of the reference value $\mathrm{AOT}_{1,\mathrm{ref}}$. To this end, a two-step numerical procedure was used. In the first step, extinction coefficient profiles at the lidar wavelengths were calculated from the inversion of the lidar signals through the implemented iterative procedure by setting the condition that extinction coefficients do not vary with altitude from the ground up to the overlap height $z_i$. Then, the AOT contribution of the $(0-z_i)$ atmospheric layer ($\mathrm{AOT}_{1,\mathrm{ref}}$) at each lidar wavelength was calculated. In the second step, extinction coefficient profiles were calculated from the implemented iterative procedure by allowing $\mathrm{AOT}_1$ to increase up to 30 % of the determined reference value $\mathrm{AOT}_{1,\mathrm{ref}}$. In fact, the condition that $\alpha(z)$ does not vary with altitude from the ground up to $z_i$ could be responsible for an underestimation of $\mathrm{AOT}_1$. The inversion of the lidar signals through the implemented iterative procedure does not demand much computation time so that a few thousand extinction profiles at 355 nm, 532 nm, and 1064 nm are easily generated by changing boundary conditions. The mean extinction profile at each lidar wavelength was then calculated by averaging all corresponding extinction profiles determined by the iterative procedure and the $\alpha(z)$ uncertainty was set equal to one standard deviation of the mean value. Ångstrom exponents at the altitude z have been calculated as follows:

$$\mathring{a}_{\lambda 1,\lambda 2}(z) = -\{\ln[\alpha_{\lambda 1}(z)/(\alpha_{\lambda 2}(z)]\}/[\ln(\lambda 1/\lambda 2)], \quad (1)$$

where $\alpha_{\lambda 1}(z)$ and $\alpha_{\lambda 2}(z)$ represent the extinction coefficient at the height $z$ and at the wavelength $\lambda 1$ and $\lambda 2$ in nm, respectively. The spectral curvature $\Delta\mathring{a}(z)$ has been set equal to the difference

$$\Delta\mathring{a}(z) = \mathring{a}_{355,532}(z) - \mathring{a}_{532,1064}(z). \quad (2)$$

Angström exponent and $\Delta\mathring{a}(z)$ profiles have been calculated for each set of the extinction profiles at 355 nm, 532 nm, and 1064 nm generated by the implemented iterative procedure. The mean profile of $\mathring{a}_{\lambda 1,\lambda 2}(z)$ and $\Delta\mathring{a}(z)$ has then been calculated and the $\mathring{a}_{\lambda 1,\lambda 2}(z)$ and $\Delta\mathring{a}(z)$ uncertainties have been set to be equal to one standard deviation of the corresponding mean value.

The linear volume depolarization ratio profile $\delta(z)$ has been calculated from the ratio of the cross-polarized to the parallel-polarized backscattering coefficient at 355 nm, and under our experimental conditions it takes the value of 0.0045 in a pure molecular atmosphere and higher values in presence of nonspherical particles as desert dust particles. Afterwards, the linear particle depolarization ratio ($\delta_p(z)$) profile (e.g. Freudenthaler et al., 2008) has been determined. $\delta(z)$ and $\delta_p(z)$ have been calculated for each cross- and parallel-polarized backscattering coefficient generated by the implemented iterative procedure. The mean $\delta_p(z)$ profile has been calculated by averaging all retrieved particle depolarization profiles and uncertainties have been set equal to one standard deviation of the mean value.

## 3 Graphical framework for the aerosol classification

To classify aerosol properties by the $\Delta\mathring{a}(z)$ vs. $\mathring{a}_{355,1064}(z)$ scatter plot, reference points corresponding to bimodal size distributions characterized by a variety of fine-mode ($R_f$) and coarse-mode ($R_c$) modal radii combined in order to lead to prescribed fine-mode fractions ($\eta$) at 532 nm were determined, according to Gobbi et al. (2007). More specifically, Mie calculations of the aerosol spectral extinction for selected $R_f$ (0.02, 0.05, 0.1, 0.15, 0.2, 0.3, and 0.4 µm) and $R_c$ (0.5, 0.6, 0.7, and 0.8 µm) values combined in order to provide $\eta$ fractions of 1, 10, 30, 50, 70, 90, 99 %, were performed. The real ($n$) and imaginary ($k$) refractive index values at 532 nm used in the Mie calculations are given in Table 1. The daily mean values of $n$ and $k$ retrieved from sun photometer AERONET measurements performed at the monitoring site of this study from 2003 to 2010 were used to calculate the mean refractive index values reported in Table 1. More specifically, the level 2, quality-assured values of $n$ and $k$ at 440, 675, and 1018 nm, respectively, were used to determine the mean values of $n$ and $k$ at 532 nm reported in Table 1. Figure 1 (black lines) shows the aerosol classification framework calculated by using $n = 1.455$ and $k = 0.0047$ at 532 nm (Table 1). Solid and dashed black lines were calculated for fixed $R_f$ values, and for fixed fine-mode fraction contributions to the total AOT at 532 nm. Figure 1 reveals that aerosol size distributions characterized by different values of the fine-mode radius and the fine-mode fractions

**Table 1.** Real ($n$) and imaginary ($k$) refractive index values at 532 nm used in the Mie simulations for mixed aerosol loads and for aerosol loads significantly affected by desert-dust intrusions ($n_c$, $k_c$) and continental pollution ($n_f$, $k_f$).

| Aerosol type | | |
|---|---|---|
| Mixed ($n$, $k$) | 1.455 | 0.0047 |
| Dust-affected ($n_c$, $k_c$) | 1.483 | 0.0035 |
| Pollution-affected ($n_f$, $k_f$) | 1.445 | 0.0070 |

can have the same $\mathring{a}_{355,1064}$, and, as a consequence, it highlights the aerosol classification framework potential.

Aerosol loads affected by Sahara dust intrusions have frequently been observed at the monitoring site of this study and characterized in a series of papers as Perrone and Bergamo (2011), Santese et al. (2008), Barnaba et al. (2004) and De Tomasi et al. (2003). It was also shown that Ångstrom exponents retrieved from AERONET sun photometer measurements provided a useful tool for identifying dust intrusion events (e.g. Santese et al., 2008). Therefore, daily mean values of $\mathring{a}_{440,675}(z) < 0.5$ were used in this study to identify the AERONET measurement days significantly affected by dust intrusion events during the years 2003 to 2010 (Perrone and Bergamo, 2011). Then, the AERONET $n$ and $k$ values (level 2, quality-assured data) retrieved during the dust-affected days were used to define the mean value of the dust-affected real ($n_c$) and imaginary ($k_c$) refractive index. $n_c$ and $k_c$ values at 532 nm are reported in Table 1 in addition to the mean value of the real ($n_f$) and the imaginary ($k_f$) refractive index found by selecting the AERONET measurements days with $\mathring{a}_{440,675}(z) > 1.2$, from 2003 to 2010 years. These last measurements days were considered to be characterized by continental pollution, according to Santese et al. (2008). The relative differences of $n_c$ and $n_f$ with $n$ (Table 1) are smaller than 2 % at 532 nm, whereas the relative differences of $k_c$ and $k_f$ with $k$ (Table 1) are smaller than 50 %. To this end, it is worth mentioning that according to Dubovik et al. (2002), the expected accuracy for the real part of the refractive index is 0.04 for AOT (440 nm) $\geq 0.5$ and of 0.05 for AOT (440 nm) $\leq 0.2$. The values of the imaginary part of the refractive index are instead retrieved with errors of the order of 30–50 % for AOT (440 nm) $\geq 0.5$ and of the order of 80–100 % for AOT (440 nm) $\leq 0.2$.

Red and blue lines in Fig. 1 represent the aerosol classification framework calculated by using the refractive index values for dust-affected ($n_c$, $k_c$) and pollution-affected ($n_f$, $k_f$) days (Table 2), and highlight the dependence of the graphical framework on refractive index values. Figure 1 shows a clockwise rotation about the origin of the constant radius curves as the real part of the refractive index increases from 1.445 to 1.483 and the imaginary part increases from 0.0035 to 0.0070. The maximum $R_f$ indetermination generated by this range of refractive indexes is of the order of ±30 % for

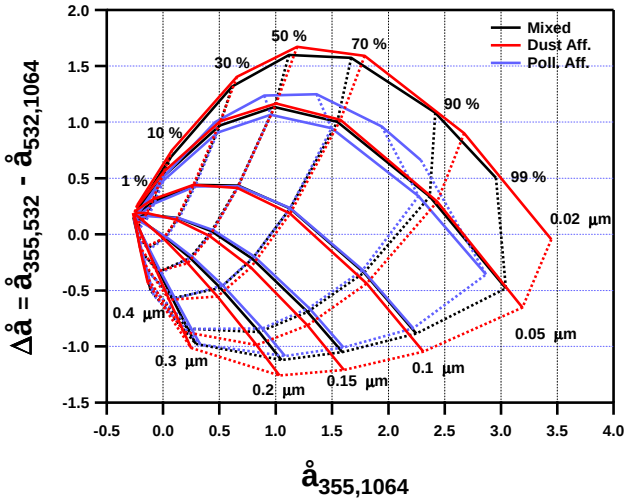


**Fig. 1.** Graphical framework for the aerosol characterization calculated according to Gobbi et al. (2007) for $n = 1.455$ and $k = 0.0047$ (black lines), $n_c = 1.483$ and $k_c = 0.0035$ (red lines), and $n_f = 1.445$ and $k_f = 0.0070$ (blue lines) at 532 nm.

$R_f \geq 0.05$ µm, whereas the maximum indetermination of $\eta$ is of the order of ±5 % for $\eta \leq 90$ %. A further test was implemented to verify the change in the generated graphical scheme of Fig. 1 (red lines) by switching from the real and imaginary refractive index values for dust reported in Table 1 to the corresponding ones recently reported by Wagner et al. (2012). The new dust refractive indices calculated from laboratory measurements on dust samples are $n_c = 1.55$ and $k_c = 0.008$. The test has shown that the average change in all the 49 grid points of Fig. 1 (red lines) was of about 7 %. These last results are in accordance with the ones reported by Gobbi et al. (2007). In fact, a sensitivity study on the effects of the refractive index changes has also been presented and discussed in Gobbi et al. (2007). The effects of changes in the coarse-mode radius have also been discussed in Gobbi et al. (2007, end of page 454).

## 4 Analysis of case studies

Some case studies are analysed in this section to demonstrate the robustness of the proposed graphical method and estimate the dependence on altitude of the fine-mode aerosol contribution and the fine-mode aerosol radius on the basis of lidar measurements of $\mathring{a}$ and $\Delta\mathring{a}$.

### 4.1 Case study: 28 July 2011

Figure 2a shows the mean extinction coefficient profiles at 355 nm (black line), 532 nm (green line), and 1064 nm (red line) retrieved from lidar measurements performed on 28 July 2011 from 12:29 to 13:00 UTC. Extinction coefficient profiles have been calculated in accordance with

**Table 2.** Lidar ratios (LR) ±1 standard deviation (SD) retrieved from the implemented iterative procedure and AOTs at the laser wavelengths. Measurement day and time interval ($T_1 - T_2$ (UTC)) during which lidar measurements were performed are also provided. The fine-mode fraction ($\eta_A$) at 500 nm, $å_{440,870}$, and $\Delta å = å_{440,675} - å_{500,870}$ values retrieved from the AERONET sun photometer measurements performed at the time $T_A$(UTC) are given in addition to the AERONET AOT at 500 nm.

| Lidar aerosol product | | | | | | | AERONET aerosol products | | | | |
|---|---|---|---|---|---|---|---|---|---|---|---|
| Day yy/mm/dd | LR ± 1 SD(sr) (wavelengths, nm) | | | AOT (wavelengths, nm) | | | $T_A$ hh:mm | $\eta_A$ at 500 nm | $å_{440,870}$ | $\Delta å$ | AOT at 500 nm |
| $(T_1 - T_2)$ | 355 | 532 | 1064 | 355 | 532 | 1064 | | | | | |
| 11/04/11 | 40 | 42 | 20 | 0.27 | 0.22 | 0.16 | 12:49 | 0.32 | 0.42 | 0.12 | 0.22 |
| 12:33–13:06 | ±4 | ±4 | ±16 | | | | | | | | |
| 11/05/30 | 39 | 36 | 31 | 0.41 | 0.24 | 0.07 | 12:15 | 0.93 | 1.55 | −0.05 | 0.26 |
| 11:59–12:31 | ±2 | ±10 | ±12 | | | | | | | | |
| 11/06/06 | 52 | 48 | 34 | 0.42 | 0.30 | 0.18 | 12:02 | 0.48 | 0.73 | 0.08 | 0.31 |
| 11:43–12:08 | ±8 | ±4 | ±11 | | | | | | | | |
| 11/06/09 | 31 | 32 | 13 | 0.33 | 0.18 | 0.05 | 12:47 | 0.79 | 1.55 | 0.12 | 0.19 |
| 12:25–12:45 | ±6 | ±3 | ±4 | | | | | | | | |
| 11/06/20 | 42 | 49 | 27 | 0.26 | 0.15 | 0.05 | 12:58 | 0.80 | 1.50 | 0.10 | 0.16 |
| 12:44–13:16 | ±4 | ±4 | ±9 | | | | | | | | |
| 11/07/28 | 50 | 45 | 11 | 0.33 | 0.20 | 0.06 | 12:40 | 0.92 | 1.51 | −0.11 | 0.21 |
| 12:28–13:00 | ±10 | ±20 | ±10 | | | | | | | | |
| 11/08/23 | 83 | 84 | 44 | 0.41 | 0.21 | 0.06 | 11:59 | 0.85 | 1.71 | −0.02 | 0.23 |
| 11:44–12:19 | ±15 | ±10 | ±16 | | | | | | | | |
| 11/08/29 | 61 | 39 | 18 | 0.67 | 0.39 | 0.12 | 11:58 | 0.84 | 1.54 | 0.00 | 0.42 |
| 11:44–12:15 | ±11 | ±4 | ±6 | | | | | | | | |
| 11/09/05 | 52 | 42 | 47 | 0.48 | 0.37 | 0.27 | 14:33 | 0.33 | 0.45 | 0.08 | 0.38 |
| 14:14–14:45 | ±10 | ±6 | ±17 | | | | | | | | |
| 11/10/03 | 67 | 64 | 17 | 0.31 | 0.15 | 0.04 | 13:08 | 0.86 | 1.83 | 0.07 | 0.17 |
| 12:41–13:16 | ±9 | ±7 | ±6 | | | | | | | | |

the methodology described in Sect. 2.2. Error bars represent uncertainties. The altitude-independent mean lidar ratio within the $(z_i - z_f)$ atmospheric layer is equal to $50 \pm 10$ sr, $45 \pm 20$ sr, and $11 \pm 10$ sr at 355 nm, 532 nm, and 1064 nm, respectively. Mean LR values ±1 SD and AOTs are reported in Table 2. AOTs are in accordance within ±0.01 with the corresponding values retrieved from the AERONET (Lecce University) sun photometer measurements at 12:40 UTC. Level 2 AERONET products have been used. The columnar fine-mode fraction ($\eta_A$) at 500 nm, $å_{440,870}$, $\Delta å = å_{440,675} - å_{500,870}$, and the AOT at 500 nm retrieved from AERONET sun photometer measurements performed at $T_A = 12{:}40$ UTC are also given in Table 2 for comparison. It is worth mentioning that $\eta_A$(500 nm) is derived from the spectral deconvolution algorithm (SDA) developed by O' Neill et al. (2003).

Aerosol particles up to ∼ 5 km a.g.l. were detected by the lidar on 28 July. In particular, a vertically inhomogeneous layering of aerosol particles was observed by the lidar from ∼ 0.5 up to 5.0 km a.g.l. The particles located within about 3–4 km a.g.l. were responsible for rather large extinction coefficients at 355 and 532 nm. The detected aerosol layering may be supported by the vertical structure of the potential temperature ($\theta$) profile (Fig. 2b, open dots) that has been obtained from radiosonde measurements performed at the meteorological station of Brindisi (http://esrl.noaa.gov/raobs/) on 28 July at 11:00 UTC. In fact, Fig. 2b reveals that the potential temperature increases with altitude and shows a temperature inversion at ∼ 2 and ∼ 4.5 km a.g.l. The radiosonde relative humidity (RH) profile shown in Fig. 2b (full dots) is also quite dependent on altitude. In particular, RH reaches the 50 % value at ∼ 2 km a.g.l., takes values ≥ 70 % within 3–4 km a.g.l., and decreases fast with altitude at $z > 4.5$ km a.g.l. This means that the particle hygroscopic growth, which varied significantly with altitude even for particles of the same type, has likely helped to obtain large extinction coefficients within 3–4 km a.g.l. The vertical profiles of the Ångstrom exponents $å_{355,532}(z)$, $å_{532,1064}(z)$, and $å_{355,1064}(z)$, and of the spectral curvature, $\Delta å(z)$, together with corresponding uncertainties, are plotted in Fig. 2c and d. $å(z)$ and $\Delta å(z)$ values retrieved at $z \geq 1$ km a.g.l. are only reported in Fig. 2b, since the lidar system is estimated to achieve full overlap at $z \geq 1$ km a.g.l. $å$ values vary with altitude and the trend is similar for all wavelength pairs. In particular, the mean $å_{355,1064}(z)$ value increases from ∼ 0.8 to 2 within 1.2–3.4 km a.g.l., and then remains constant up to ∼ 4.6 km a.g.l. $\Delta å$ mean values vary from −0.8 to 0.0 within the 1–4.6 km a.g.l. The change with the altitude of

the aerosol size distribution and hence of the aerosol properties is responsible for the dependence of $\mathring{a}_{\lambda1,\lambda2}(z)$ and $\Delta\mathring{a}(z)$ on $z$ and for the changes of $\mathring{a}_{\lambda1,\lambda2}(z)$ with the wavelength pair. Note that the efficiency of scattering by small particles reaches the maximum value when the size parameter is comparable with the wavelength; thus the scattering of small particles is more pronounced at the short wavelengths, and the scattering of the large particles is more pronounced at long ones (Lopatin et al., 2013). As a consequence, Ångstrom exponent values are quite dependent on the wavelength pairs used, as Fig. 2c clearly reveals. Figure 2c shows that $\mathring{a}_{532,1064}(z)$ is larger than $\mathring{a}_{355,532}(z)$ mainly at $z \geq 2$ km a.g.l. The larger value of extinction coefficient $\alpha_{532}(z)$ with respect to that of $\alpha_{1064}(z)$ is responsible for this result (Eq. 1): this is expected to occur when fine-mode particles are dominant, in accordance with the above statement. The blue line in Fig. 2e represents the linear particle depolarization ratio ($\delta_p(z)$) profile with corresponding uncertainties. $\delta_p(z)$ was calculated from the measured linear volume depolarization ratio (e.g. Freudenthaler et al., 2008) as has been outlined in Sect. 2.2. It reaches greater values within 1–2 km a.g.l. This last result indicates that the contribution of nonspherical particles was largest within 1–2 km a.g.l. Calculated $\Delta\mathring{a}(z)$ vs. $\mathring{a}_{355,1064}$ $(z)$ values are plotted in Fig. 3a (open dots) with corresponding uncertainties. Different colours are used to represent $\Delta\mathring{a}(z) - \mathring{a}_{355,1064}$ $(z)$ values referring to different $z$, as indicated by the colour bar on the top of Fig. 3a. The graphical framework calculated for $n = 1.455$ and $k = 0.0047$ at 532 nm is shown in Fig. 3a. These refractive index values were considered representative of aerosol loads affected by mixed aerosol types, in accordance with the discussion reported in the previous section. Figure 3a (open dots) shows that the $\mathring{a}_{355,1064}(z) - \Delta\mathring{a}(z)$ mean values within 1–2 km a.g.l. are on the graphical framework area delimited by $\eta$ equal to about 60 % and 80 %, respectively, and $R_f$ equal to $\sim 0.10$ µm and 0.15 µm, respectively. Conversely, the $\mathring{a}_{355,1064} - \Delta\mathring{a}$ mean values within 3.5–4.6 km a.g.l. are located on the framework area delimited by $\eta$ equal to 90 % and 99 %, respectively, and $R_f$ equal to 0.08 µm and 0.12 µm, respectively. These results, which can allow one to obtain an estimate of $\eta(z)$ and $R_f(z)$, indicate that the contribution of fine-mode particles to the whole aerosol load progressively increases with the altitude, while the fine-mode radius decreases with the altitude.

Analytical back trajectories from the Hybrid Single Particle Lagrangian Integrated Trajectory Model (HYSPLIT) (Draxler and Rolph, 2003) were used to gain information about the source regions of the air masses advected over south-eastern Italy on 28 July 2011 and to understand and/or support the $\eta(z)$ and $R_f(z)$ variability range resulting from the $\Delta\mathring{a}(z)$-$\mathring{a}(z)$ scatter plot. Figure 4a shows the pathways estimated at 13:00 UTC of the ten-day back trajectories with arrival heights at 1, 2, and 4 km a.g.l. The time evolution of the altitude of each back trajectory is plotted in Fig. 4b. North America was the source region of the air masses arriving from 1 up to 4 km a.g.l. The air masses arriving at 4 km a.g.l have travelled at altitudes varying within 3–6 km a.g.l. before reaching south-eastern Italy. By contrast, the air masses at 2 km arrival height crossed north-western Africa before

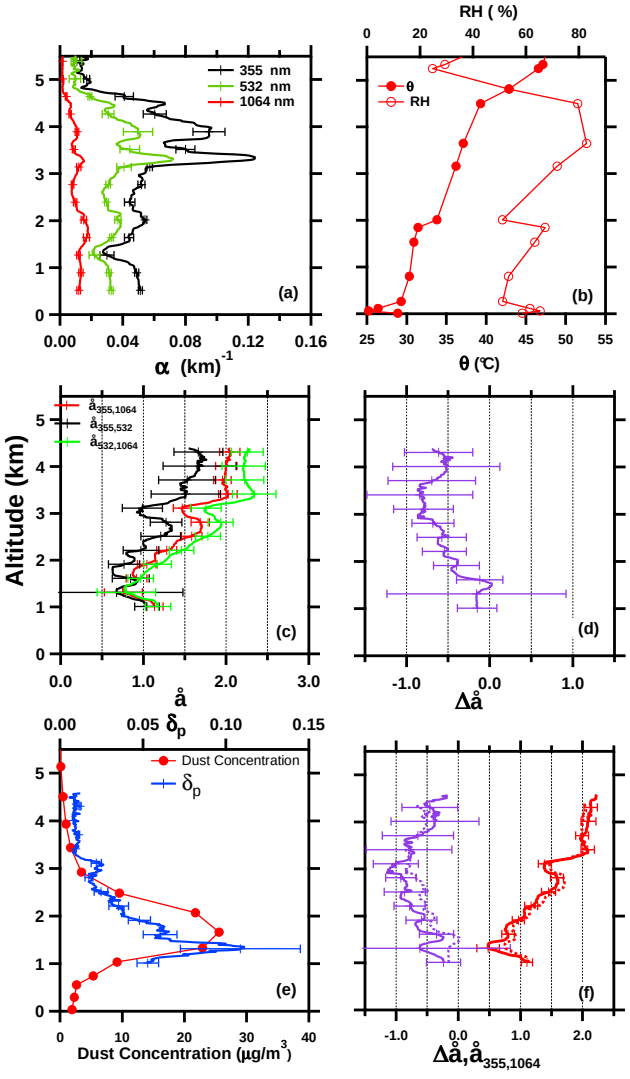


**Fig. 2. (a)** Extinction coefficient profiles at 355 nm (black line), 532 nm (green line), and 1064 nm (red line) retrieved from lidar measurements performed on 28 July 2011 from 12:28 to 13:00 UTC. **(b)** Vertical profiles of the potential temperature ($\theta$) and relative humidity (RH) retrieved from radio-sounding measurements performed at 11:00 UTC. Vertical profiles of **(c)** the Ångstrom exponents $\mathring{a}_{355,532}(z)$, $\mathring{a}_{532,1064}(z)$, $\mathring{a}_{355,1064}(z)$, and **(d)** the spectral curvature $\Delta\mathring{a}(z)$. **(e)** Vertical profile of the linear particle depolarization ratio (blue line) with corresponding uncertainties (error bars) and the dust particle concentration from the BSC–DREAM model (red line). **(f)** Vertical profiles of the Ångstrom exponents $\mathring{a}_{355,1064}(z)$ and the spectral curvature $\Delta\mathring{a}(z)$ calculated from extinction profiles based on altitude-dependent lidar ratio values. Dotted lines represent the corresponding profiles plotted in Fig. 2c and d, respectively.

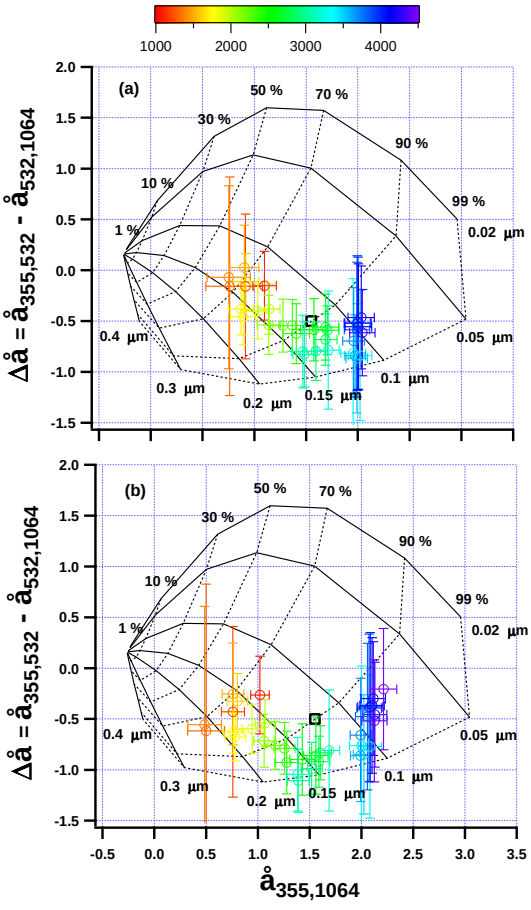


**Fig. 3.** Solid and dashed black lines represent the graphical framework calculated for $n = 1.455$ and $k = 0.0047$ at 532 nm. **(a)** Open dots represent calculated $\Delta\mathring{a}(z)$ vs. $\mathring{a}(z)$ values. Error bars represent uncertainties. Different colours are used to represent $\Delta\mathring{a}(z)$-$\mathring{a}(z)$ values referring to different $z$, as indicated by the colour bar on the top of the figure. The full black box represents the columnar $\mathring{a}_{in}(355, 1064)$ and $\Delta\mathring{a}_{in}$ values calculated from Eq. (4)–(5), respectively. **(b)** Open dots represent $\Delta\mathring{a}(z)$ vs. $\mathring{a}(z)$ values calculated from extinction profiles based on altitude-dependent lidar ratio values.

reaching south-eastern Italy and, as a consequence, they likely picked up lofted desert dust particles. In fact, dust particles lifted up to a few kilometres a.g.l. are commonly subject to long-range transport. The true colour images from the Moderate Resolution Imaging Spectroradiometer (MODIS) on board the Terra and Aqua satellite support the last comment. The MODIS images reveal the presence of African dust particles over the south-western Mediterranean both at 11:35 UTC (http://lance-modis.eosdis.nasa.gov/cgi-bin/imagery/single.cgi?granule=T112071035) and at 12:10 UTC (http://lance-modis.eosdis.nasa.gov/cgi-bin/imagery/single.cgi?granule=A112071210) of 26 July 2011 and Fig. 4b indicates that the 2 km air masses have likely crossed the south-western Mediterranean on 26 July. The BSC–DREAM model also simulated the advection of a small amount of Sahara dust particles over south-eastern Italy. For the monitoring site of this study, it predicted the existence of a dust layer within 0.5–3 km a.g.l. at 12:00 UTC. Figure 2e (red line) shows the vertical profile of the dust particle concentration from the BSC–DREAM model (http://www.bsc.es/earth-sciences/mineral-dust-forecast-system/bsc-dream8b-forecast/north-africa-europe-and-middle-ea-0): the dust particle concentration varies up to $\sim 25\,\mu g\,m^{-3}$ within 0.5–3.0 km a.g.l. Thus, the greater $\delta_p(z)$ values retrieved from lidar measurements within 1–2 km a.g.l. (Fig. 2e, blue line) are likely due to the contribution of desert dust particles, in accordance with MODIS images and the BSC–DREAM simulations. It is also interesting to observe that the extinction coefficients at 355 nm, 532 nm, and 1064 nm (Fig. 2a) reach a peak value at $\sim 2$ km a.g.l. Hence, the contribution of desert dust particles has likely helped to obtain up to $\sim 2$ km a.g.l. $\eta(z)$ and $R_f(z)$ values smaller and larger, respectively, than the corresponding ones obtained for the aerosol load located at $z > 2$ km a.g.l. The $\eta(z)$ and $R_f(z)$ mean values within 3.0–4.6 km a.g.l., which vary from 90 % to 99 % and from 0.08 µm to 0.15 µm, respectively, are likely due to anthropogenic pollution lifted up to altitudes $z > 2$ km a.g.l. and then transported over south-eastern Italy in accordance with Fig. 4. Typical size distribution associated with desert dust and continental pollution support the last statements (Seinfeld and Pandis, 1998).

The black box in Fig. 3a represents the columnar $\Delta\mathring{a}_{in}$ and $\mathring{a}_{in}(355, 1064)$ values calculated from the AOTs at 355, 532, and 1064 nm using the following relationships:

$$\mathring{a}_{in}(\lambda_1, \lambda_2) = -\{\ln AOT_{\lambda 1}/AOT_{\lambda 2}]\}/[\ln(\lambda_1/\lambda_2)], \quad (3)$$

$$\Delta\mathring{a}_{in} = \mathring{a}_{in}(355, 532) - \mathring{a}_{in}(532, 1064). \quad (4)$$

We found that $\Delta\mathring{a}_{in} = -0.5$ and $\mathring{a}_{in}$ (355, 1064) $= 1.5$. These values correspond to $\eta_{in} \cong 0.9$ and $R_{f-in} \cong 0.12$ µm, which can be considered typical of continental pollution (Seinfeld and Pandis, 1998). $\eta_{in}$ is in good accordance with the value of $\eta_A(550\,nm) = 0.92$ retrieved from AERONET sun photometer measurements. It is interesting to note that $\Delta\mathring{a}_{in}$ and $\mathring{a}_{in}(355, 1064)$ values are closest to the $\Delta\mathring{a}(z)$ and $\mathring{a}_{355,1064}(z)$ values that characterize the aerosol load at $z > 3$ km a.g.l. In fact, Fig. 2a combined with Fig. 3a indicate that AOTs have mainly been driven by the fine-mode particle contribution at 532 nm and 355 nm, respectively. $\Delta\mathring{a}_{in}$ and $\mathring{a}_{in}(355, 1064)$ values highlight the differences which may occur between vertically resolved and column-integrated $\eta$ and $R_f$ values. In particular, Fig. 3a shows that the $\Delta\mathring{a}_{in} - \mathring{a}_{in}$ data point (black box) may lead to the underestimation of $\eta(z)$ and the overestimation of $R_f(z)$ at $z > 3$ km, and to the overestimation of $\eta(z)$ and the underestimation of $R_f(z)$ at $z < 2$ km. The differences between vertical-resolved and column-integrated $\eta$ and $R_f$ values are expected to be quite large when aerosols of a different type/origin are located at

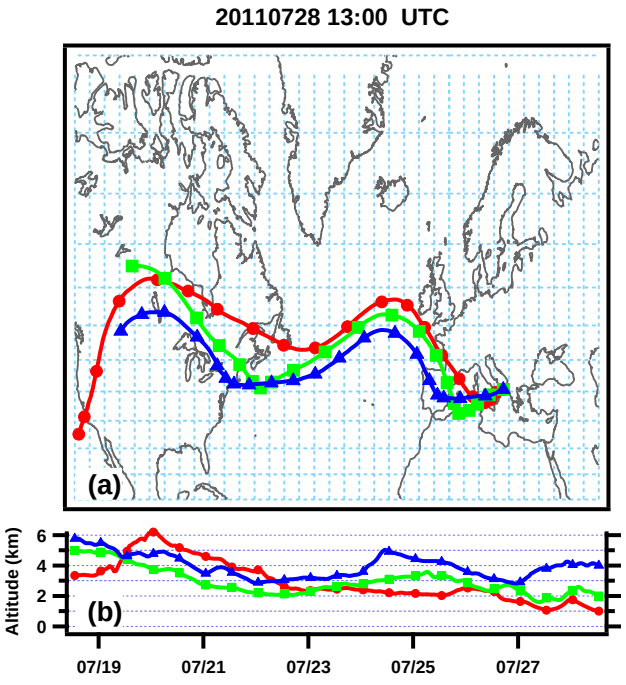


**Fig. 4. (a)** Pathways estimated at 13:00 UTC on 28 July 2011, of the ten day HYSPLIT back trajectories with arrival heights at 1, 2, and 4 km a.g.l. **(b)** Time evolution of the altitude of each back trajectory.

different altitudes, as occurred in the study case of this section. Note that aerosols from continental Europe, the Atlantic Ocean and the Mediterranean Sea, and African deserts are frequently advected over the monitoring site of this study and more generally all over the central Mediterranean, as the case study of this section has revealed. As a consequence, aerosol size distributions may significantly vary with the altitude over the central Mediterranean, and this must be accounted for in radiative transfer simulations (Perrone et al., 2012).

#### 4.1.1 Sensitivity test on the lidar ratio vertical profile for 28 July 2011

Figure 3a and the discussion in the previous section reveal that the aerosol size distribution may significantly vary with altitude when aerosols of different types (i.e. origins) are located at different altitudes. In fact, lidar measurements combined with additional information have revealed that the aerosol particles within 1–2 km a.g.l. have likely been affected by Saharan dust on 28 July 2011. By contrast, it has been found that fine-mode particles, likely due to continental pollution, were prevailing within 3.5–4.6 km a.g.l. Lidar ratios values depend on aerosol optical and microphysical properties, and, as a consequence, they vary with the aerosol type. Thus, the use of altitude-independent lidar ratios to retrieve the extinction lidar profiles at 355, 532, and 1064 nm, (as described in the previous section) represents a weak point of the performed analysis. Lidar ratios dependent on altitude are used in this section to test the sensitivity of the $\Delta\mathring{a}(z) - \mathring{a}_{355,1064}(z)$ scatter plot on lidar ratios for the case study of 28 July 2011. More specifically, we have hypothesized that the assumption of altitude-independent lidar ratios was responsible for the overestimation of the aerosol optical thickness due to the aerosol located up to 2 km a.g.l. ($AOT_{inf}$) and the underestimation of the AOT due to the aerosol located at $z > 2$ km a.g.l. ($AOT_{sup}$), which was likely more affected by anthropogenic pollution. As an example, we have assumed that the aerosol optical thickness due to the aerosol located at $z > 2$ km a.g.l. was 20 % larger than the corresponding value found with altitude-independent LRs ($AOT_{sup,ref}$). Subsequently, extinction coefficient profiles at 355, 532, and 1064 nm were calculated from the implemented iterative procedure by setting the condition that $AOT_{sup} = (AOT_{sup,ref} + 0.2 \times AOT_{sup,ref})$ and by leaving the aerosol optical thickness due to the whole aerosol layer unchanged. We found from the implemented iterative procedure that lidar ratios equal to $80 \pm 20$ sr, $60 \pm 30$ sr, and $20 \pm 20$ sr at 355 nm, 532 nm, and 1064 nm, respectively, at $z > 2$ km a.g.l., and equal to $40 \pm 15$ sr, $20 \pm 15$ sr, and $6 \pm 2$ sr at 355 nm, 532 nm, and 1064 nm, respectively, at $z \leq 2$ km a.g.l., were required to fulfil the above reported assumption regarding $AOT_{sup}$ and $AOT_{inf}$. Note that lidar ratio values at 351 nm even larger than 100 sr were retrieved over south-eastern Italy during the advection of continental pollution, according to Barnaba et al. (2007). On the contrary, lidar ratios even equal to $\sim 20$ sr at 351 nm were retrieved over south-eastern Italy for dust-polluted aerosol loads (Barnaba et al., 2004). Figure 2f (solid lines) shows the vertical profiles of $\Delta\mathring{a}(z)$ and $\mathring{a}_{355,1064}(z)$ retrieved when LRs at $z > 2$ km a.g.l. are larger than the corresponding ones at $z \leq 2$ km a.g.l. The dotted lines in Fig. 2f show for comparison the vertical profile of $\Delta\mathring{a}(z)$ and $\mathring{a}_{355,1064}(z)$ retrieved from the altitude-independent LRs. It is interesting to note that the differences between the solid and the corresponding dotted profile are on average smaller than the solid profile uncertainties. Figure 3b shows $\Delta\mathring{a}(z)$ vs. $\mathring{a}_{355,1064}(z)$ with corresponding uncertainties (error bars). The comparison of Fig. 3b with Fig. 3a reveals that the use of smaller (larger) LRs at $z \leq 2$ km a.g.l. ($z > 2$ km a.g.l.) has not significantly affected the $\Delta\mathring{a}(z)$ vs. $\mathring{a}_{355,1064}(z)$ scatter plot: the main differences are due to the fact that $\Delta\mathring{a}(z)$ takes, on average, smaller and larger values within 1–3 km and 3.5–4.6 km a.g.l., respectively, when LRs vary with altitude. The following methodology is suggested to select altitude-dependent lidar ratios, in accordance with the above reported analysis. Altitude-independent LRs could at first have been assumed to obtain a first guess on the $\Delta\mathring{a}(z)$ and $\mathring{a}_{355,1064}(z)$ profiles and the corresponding $\eta(z)$ and $R_f(z)$ values. Then, if the proposed graphical approach combined with additional experimental and model data will allow inferring the dependence on $z$ of the main aerosol types and hence of the prevailing lidar ratios values, it would be preferable to

recalculate $\Delta\mathring{a}(z)$ and $\mathring{a}_{355,1064}(z)$ profiles from extinction profiles based on altitude-dependent LRs, to reduce the uncertainties of $\eta(z)$ and $R_f(z)$ values. However, the selection of altitude-dependent LRs can also be responsible for large extinction and AOTs uncertainties, since LRs depend on the source regions of the aerosol particles and on the pathways the aerosols crossed before reaching the monitoring site (e.g. Barnaba et al., 2004, 2007; De Tomasi et al., 2006). The coexistence of different aerosol types in one layer can also give rise to considerable uncertainty in the lidar ratio value and its impact on the AOT. Because of this, we decided to use altitude-independent LRs in the case studies analysed in this paper. We believe that the uncertainties of the $\eta(z)$ and $R_f(z)$ values due to the assumption of an altitude-independent LR would be comparable, in most of the case studies, to the ones resulting from an inappropriate choice of LR values dependent on altitude, as a consequence of the addressed problems.

### 4.2 Case study: 29 August 2011

Lidar measurements performed on 29 August 2011 are analysed in this case study to further test the capability of the proposed graphical method. Fig. 5a shows the extinction coefficient profile at 355 nm (black line), 532 nm (green line), and 1064 nm (red line) retrieved from lidar measurements performed from 11:44 to 12:19 UTC by using the implemented iterative procedure (Sect. 2.2). Error bars represent uncertainties. The retrieved altitude-independent lidar ratios are equal to $61 \pm 11$ sr, $39 \pm 4$ sr, and $18 \pm 6$ sr at 355 nm, 532 nm, and 1064 nm, respectively, from $z_i = 0.5$ km to $z_f = 6$ km a.g.l. Mean LR values and calculated AOTs are in Table 2. AOTs are in accordance, within $\pm 0.01$, with the corresponding ones retrieved from the AERONET sun photometer measurements at 11:58 UTC. A vertically inhomogeneous layering of aerosol particles was observed with the lidar from $\sim 0.5$ up to 4 km a.g.l. The potential temperature and RH profiles (Fig. 5b) obtained from radiosonde measurements performed on 29 August at 11:00 UTC support the aerosol layering. $\theta$ (Fig. 5b, full dots) decreases with altitude at $z > 0.5$ km a.g.l. and shows a marked temperature inversion at $\sim 0.7$, 1.8, and 3.5 km a.g.l., respectively. RH that is equal to 40 % at $\sim 1.8$ km a.g.l. increases with altitude up to $\sim 3.5$ km a.g.l., where it reaches the value of $\sim 70$ %, and then rapidly decreases (Fig. 5b, open dots). Figure 5c and d show the vertical profiles of $\mathring{a}_{355,532}(z)$, $\mathring{a}_{532,1064}(z)$, and $\mathring{a}_{355,1064}(z)$ and of the spectral curvature $\Delta\mathring{a}(z) = \mathring{a}_{355,532}(z) - \mathring{a}_{532,1064}(z)$, respectively, with corresponding uncertainties. We observe that $\mathring{a}_{355,532}(z)$ mean values span the 0.9–1.7 range and increase with altitude within 2–3 km a.g.l. $\mathring{a}_{355,1064}(z)$ which spans the 1.5–1.8 range, is characterized by a weaker dependence on $z$, and increases with altitude within 1.5–3 km a.g.l. $\Delta\mathring{a}(z)$ takes negative values spanning the $-1$–0 range within 1–3.5 km a.g.l. Open dots and error bars in Fig. 6 show the scatter plot of $\Delta\mathring{a}(z)$ vs. $\mathring{a}_{355,1064}(z)$ with corresponding uncertainties of the graphical framework

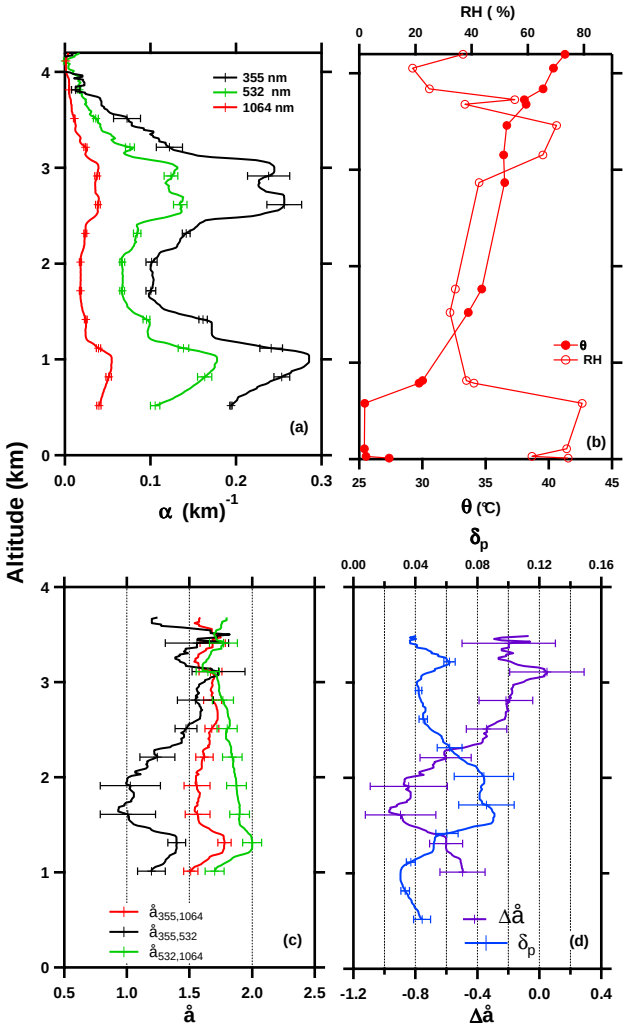


**Fig. 5.** Extinction coefficient profile at 355 nm (black line), 532 nm (green line), and 1064 nm (red line) retrieved from lidar measurements performed on 29 August 2011 from 11:44 to 12:19 UTC. **(b)** Vertical profiles of potential temperature ($\theta$) and relative humidity (RH) retrieved from radio sounding measurements performed at 11:00 UTC. Vertical profiles of **(c)** the Ångstrom exponents $\mathring{a}_{355,532}(z)$, $\mathring{a}_{532,1064}(z)$, and $\mathring{a}_{355,1064}(z)$ and **(d)** the spectral curvature $\Delta\mathring{a}(z)$. The blue line in Fig. 5d represents the vertical profile of the linear particle depolarization ratio.

calculated for $n = 1.455$ and $k = 0.0047$ at 532 nm. Figure 6 reveals that the $\mathring{a}$–$\Delta\mathring{a}$ data points within 1–2 km a.g.l. lie mainly on the graphical framework area delimited by $\eta$ equal to 90 % and 99 %, and $R_f$ equal to 0.12 µm and 0.15 µm, respectively. The $\mathring{a}$–$\Delta\mathring{a}$ data points at altitudes higher than 2.5 km a.g.l. are mainly located on the area delimited by $\eta$ equal to 80 % and 90 %, and $R_f$ equal to 0.08 µm and 0.1 µm. These results indicate that fine-mode particles prevailed on 29 August all along the aerosol column, in good accordance with the value of $\eta_A(500\,\text{nm}) = 0.84$ retrieved from the SDA applied to sun photometer measurements (O' Neill et al.,

2003). However, we believe that Fig. 6 (open dots) can allow the inference that the size distribution of the aerosol particles located at $z > 2$ km a.g.l. was characterized by a smaller fine-mode radius and fine-mode fraction than the one due to the particles located at $z < 2$ km a.g.l. HYSPLIT analytical back trajectories were used to know about the source regions of the air masses advected over south-eastern Italy on 29 August 2011 and to understand and support the aerosol microphysical properties revealed by Fig. 6. Figure 7a shows the pathways estimated at 12:00 UTC of the ten-day back trajectories with arrival heights at 1, 2, and 3 km a.g.l. The time evolution of the altitude of each back trajectory is plotted in Fig. 7b. Air masses from north-eastern Europe were advected to south-eastern Italy on 29 August at 12:00 UTC. Advection patterns similar to the one in Fig. 7a are rather frequent over south-eastern Italy mainly in summer, according to Perrone et al. (2013) and Santese et al. (2008). It was also shown by Perrone et al. (2013) that the air flows from north-eastern Europe were mainly responsible for the advection of fine-mode particles due to ammonium sulfate (Fig. 6b in Perrone et al., 2013), traffic (Fig. 6f in Perrone et al., 2013), and combustion including biomass burning (Fig. 7a in Perrone et al., 2013) sources. Lelieveld et al. (2002) also revealed the important contribution of fine pollution aerosols transported from central and eastern Europe to south-eastern Italy, in satisfactory agreement with the results from Fig. 6 (open dots). It is worth noting from Fig. 7b that the 1, 2, and 3 km arrival-height back trajectories were close to the ground level over Eastern Europe and as a consequence, they were likely responsible for the lifting of soil particles up $\sim 3$ km a.g.l. The lack of rainy days mainly occurring in summer over southern Europe also enhances the natural and anthropogenic dust resuspension. Finally, it is worth mentioning that the true colour image from the Moderate Resolution Imaging Spectroradiometer (MODIS) on board the Aqua satellite revealed the presence of a thin layer of African dust particles over south-eastern Italy at 12:00 UTC of 29 August 2011 (http://lance-modis.eosdis.nasa.gov/cgi-bin/imagery/single.cgi?granule=A112411200). Hence, resuspended soil and/or desert dust particles have likely contributed to the decrease of $\eta(z)$ with the altitude revealed by Fig. 6. The linear particle depolarization ratio profile (Fig. 5d, blue line) retrieved from lidar measurements support the last comments: $\delta_p(z)$ takes values spanning the 0.06–0.09 range within about 1.5–2.5 km a.g.l. The black open box in Fig. 6 represents $\mathring{a}_{in}$ (355, 1064) $= 1.6$ and $\Delta\mathring{a}_{in} = -0.36$, which have been calculated in accordance with Eqs. (4)–(5), respectively, and corresponds to $\eta_{in} \cong 0.9$ and $R_{f-in} \cong 0.1$ µm. Note that the $\mathring{a}(z) - \Delta\mathring{a}(z)$ data points in Fig. 6 (open dots) are less spread out than the ones in Fig. 3. As a consequence, the differences between $R_f(z)$ and $R_{f-in}$ and $\eta(z)$ and $\eta_{in}$ are smaller than the corresponding ones revealed by Fig. 3.

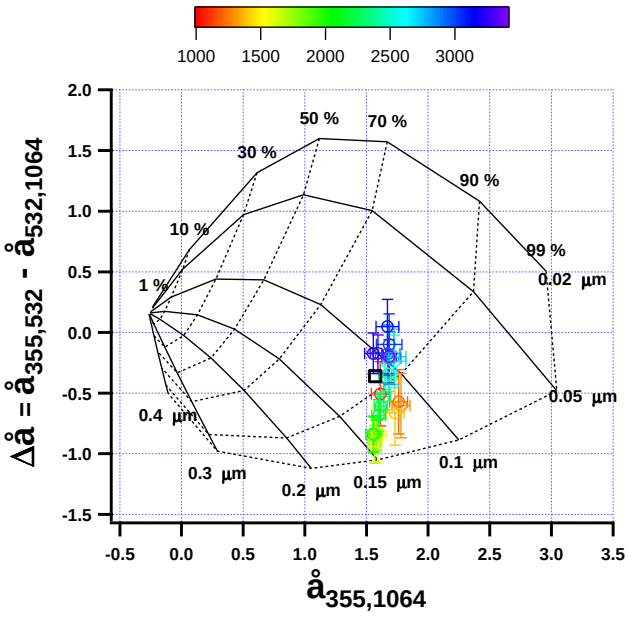


**Fig. 6.** Scatter plot of $\Delta\mathring{a}(z)$ vs. $\mathring{a}_{355,1064}(z)$ retrieved from the lidar measurements performed on 29 August 2011 within 11:44–12:19 UTC. Different colours represent different altitudes in accordance with the colour bar on the top. The open black box represents the $\Delta\mathring{a}_{in}$ and $\mathring{a}_{in}$(355, 1064) data point.

### 4.3 Case study: 5 September 2011

Figure 8a shows the extinction coefficient vertical profiles at 355, 532, and 1064 nm retrieved from the lidar measurements performed on 5 September 2011 from 14:14 to 14:45 UTC. Error bars represent uncertainties. Mean lidar ratios retrieved from the implemented iterative procedure (Sect. 2.2) are $52 \pm 10$ sr, $42 \pm 6$ sr, and $47 \pm 17$ sr at 355 nm, 532 nm, and 1064 nm, respectively, (Table 2). A vertically inhomogeneous layering of aerosol particles was observed with the lidar from $\sim 0.5$ up to 5.0 km a.g.l., on 5 September 2011. The potential temperature ($\theta$) profile that increases with $z$ (Fig. 8b, full dots) supports the detected aerosol layering. $\theta$ was obtained from radio-sounding measurements performed at 11:00 UTC of 5 September 2011. The radiosonde relative humidity (RH) profile is also shown in Fig. 8b (open dots), and it is interesting to note that the RH takes values $\geq 80$ % within 3.5–4.8 km a.g.l. (De Tomasi and Perrone, 2003; Perrone et al., 2012). The vertical profiles of the Ångstrom exponents $\mathring{a}_{355,532}(z)$, $\mathring{a}_{532,1064}(z)$, and $\mathring{a}_{355,1064}(z)$, and of the spectral curvature $\Delta\mathring{a}(z)$ with corresponding uncertainties are plotted in Fig. 8c and d. $\mathring{a}_{355,1064}(z)$ and $\Delta\mathring{a}(z)$ vary within 0.1–0.5 and 0.0–0.9 from 1 up to 4 km a.g.l. In Fig. 8c, it is worth noting that $\mathring{a}_{355,532}(z)$ is larger than $\mathring{a}_{355,1064}(z)$ at $2 < z < 3.3$ km a.g.l. This result can be due to a significant contribution of coarse-mode particles within 2–3.3 km a.g.l., in accordance with the discussion reported in Sect. 4.1. $\Delta\mathring{a}(z)$ vs. $\mathring{a}_{355,1064}$ $(z)$ mean values are

plotted in Fig. 9 (open dots) with corresponding uncertainties. $\mathring{a}_{355,1064}(z) - \Delta\mathring{a}(z)$ mean values within 1–3.5 km a.g.l. are mainly on the graphical framework area delimited by $\eta$ equal to 30 % and 50 %, and $R_f$ equal to $\sim 0.05$ µm and 0.2 µm, whereas the $\mathring{a}_{355,1064}(z) - \Delta\mathring{a}(z)$ mean values within 3.5–4.5 km a.g.l. are mainly on the graphical framework area delimited by $\eta$ equal to 50 % and 70 %, and $R_f$ equal to $\sim 0.1$ µm and 0.2 µm. These results reveal the prevailing contribution of coarse-mode particles within 1–3.5 km a.g.l. Figure 8e shows the linear particle depolarization ratio profile and we observe that $\delta_p(z)$ reaches mean values larger than 0.15 from 1 up to 4.5 km a.g.l. Then, coarse nonspherical particles, like the ones due to desert dust, have likely affected the whole aerosol load. Mean lidar ratio values at 355 nm, 532 nm, and 1064 nm, (Table 2), support the last statements (e.g. Muller et al., 2007). The HYSPLIT analytical back trajectories (Fig. 10a–b) reaching south-eastern Italy on 5 September 2011 at 11:00 UTC also support the advection of desert dust particles. Air masses that on 3 and 4 September crossed north-western Africa at low altitudes (1–2 km a.g.l.) were directly advected over south-eastern Italy on 5 September (14:00 UTC), from about 1 to 4 km a.g.l. It is interesting to note that, for the monitoring site of this study, the BSC–DREAM model simulated the existence of a dust layer from the ground up to $\sim 5$ km a.g.l. at 12:00 UTC (Fig. 8f) with dust concentrations reaching the largest values ($\cong 100\ \mu g\ m^{-3}$) within 3.0–3.5 km a.g.l. Note that extinction coefficient profiles (Fig. 8a) reached a peak value at $\sim 2.9$ km a.g.l., in satisfactory accordance with the modelled dust concentration profile. MODIS, on board the Aqua satellite, also revealed the presence of dust over the central Mediterranean on 5 September 2011 at 12:05 UTC (http://lance-modis.eosdis.nasa.gov/cgi-bin/imagery/single.cgi?granule=A112481205) Hence, $\delta_p(z)$, the MODIS true colour image, the HYSPLIT analytical back trajectories, and the BSC–DREAM model all support the $\eta(z)$ and $R_f(z)$ mean values and, to some extent, their respective dependence on $z$ retrieved from the graphical framework of Fig. 9 (open dots). AERONET sun photometer measurements also support the results revealed by Fig. 9: $\eta_A$(500 nm) and $\mathring{a}_{440,870}$ reached rather small values (0.33 and 0.45, respectively) on 5 September 2011 (Table 2).

### 4.4 Case study: 3 October 2011

The extinction coefficient vertical profiles at 355, 532, and 1064 nm, respectively, retrieved from lidar measurements performed on 3 October 2011 from 12:41 to 13:16 UTC are plotted in Fig. 11 with corresponding uncertainties (error bars). Mean lidar ratios retrieved from the implemented iterative procedure (Sect. 2.2) are $67 \pm 9$ sr, $64 \pm 7$ sr, and $17 \pm 6$ sr at 355 nm, 532 nm, and 1064 nm, respectively (Table 2). A vertically homogeneous layering of aerosol particles was detected from the lidar within 1–2.5 km a.g.l. The potential temperature (full dots) and the RH (open dots) profiles shown in Fig. 11b support the $\alpha(z)$ profiles. $\theta$ and RH have been retrieved from radio-sounding measurements performed at 11:00 UTC on 3 October and Fig. 11b reveals that $\theta$ shows a marked inversion at $\sim 0.7$ and 2.5 km a.g.l. The vertical profiles of the Ångstrom exponents $\mathring{a}_{355,532}(z)$, $\mathring{a}_{532,1064}(z)$, and $\mathring{a}_{355,1064}(z)$, and of the spectral curvature $\Delta\mathring{a}(z)$ together with corresponding uncertainties are plotted in Fig. 11c and d, respectively. Figure 11c reveals that the $\mathring{a}_{355,1064}(z)$ mean values span the 1.9–2.1 range from 1 up to 2.5 km a.g.l. $\mathring{a}_{355,532}(z)$ is smaller than $\mathring{a}_{355,1064}(z)$ at all altitudes and decreases faster than $\mathring{a}_{355,1064}(z)$ with the increase of $z$ up to $\sim 2.5$ km a.g.l. The increase with the altitude of the particle size is likely responsible for this result, in accordance with the discussion reported in Sect. 4.1. $\Delta\mathring{a}(z)$ mean values are negative and decrease with altitude (Fig. 11d) spanning the – (0.2–1.1) range within 1–2.5 km a.g.l. Calculated $\Delta\mathring{a}(z)$ vs. $\mathring{a}_{355,1064}$ $(z)$ values are plotted in Fig. 9 (open triangles) together with corresponding uncertainties. $\mathring{a}_{355,1064}(z)$-$\Delta\mathring{a}(z)$ mean values are on the graphical framework area delimited by $\eta$ equal to 90 % and 99 %, and $R_f$ values equal to $\sim 0.08$ µm and 0.12 µm, respectively. These results reveal the prevailing contribution of fine-mode particles on 3 October. The HYSPLIT analytical back trajectories reaching south-eastern Italy on 3 October 2011 at 13:00 UTC are plotted in Fig. 12a–b. We observe that air masses that crossed anthropized areas of north-eastern Europe were advected at the monitoring site of this study from about 1 to

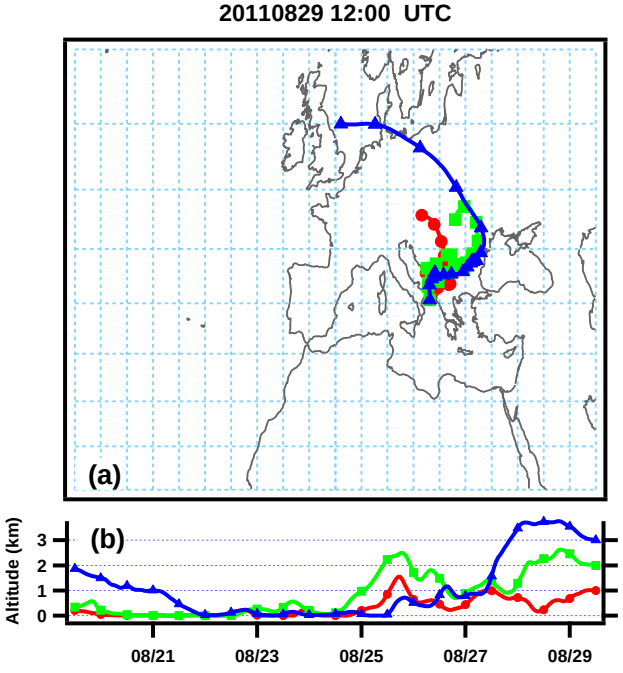


**Fig. 7. (a)**Pathways of the ten-day HYSPLIT back trajectories of 29 August 2011 estimated at 12:00 UTC, each with arrival heights at 1, 2, and 3 km a.g.l. **(b)**Time evolution of the altitude of each back trajectory.

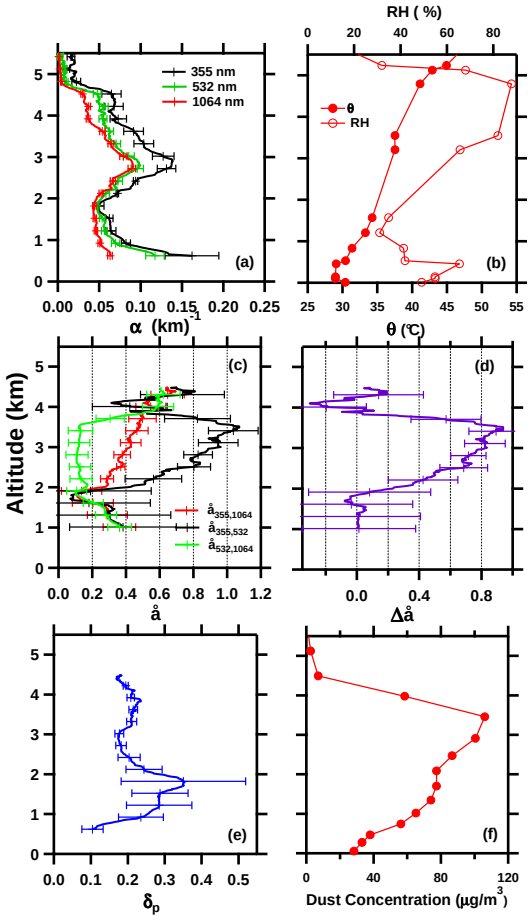


**Fig. 8. (a)** Extinction coefficient profiles at 355 nm (black line), 532 nm (green line), and 1064 nm (red line) retrieved from lidar measurements performed on 5 September 2011 from 14:14 to 14:45 UTC. **(b)** Vertical profiles of potential temperature ($\theta$) and relative humidity (RH) retrieved from radio sounding measurements performed at 11:00 UTC. Vertical profiles of **(c)** the Ångstrom exponents $\mathring{a}_{355,532}(z)$, $\mathring{a}_{532,1064}(z)$, $\mathring{a}_{355,1064}(z)$, and **(d)** the spectral curvature $\Delta\mathring{a}(z)$. **(e)** Vertical profile of the linear particle depolarization ratio (blue line) with corresponding uncertainties (error bars). **(f)** Dust particle concentration from the BSC–DREAM model.

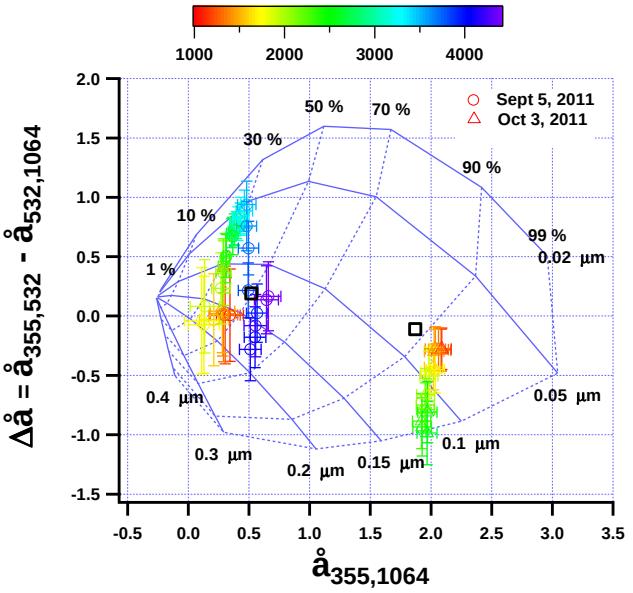


**Fig. 9.** $\Delta\mathring{a}(z)$ vs. $\mathring{a}_{355,1064}$ $(z)$ scatter plot with corresponding uncertainties retrieved from lidar measurements performed on 5 September 2011 from 14:14 to 14:45 UTC (open dots) and on 3 October 2011 from 12:41 to 13:16 UTC (open triangles). The open black boxes represent the $\Delta\mathring{a}_{\mathrm{in}}$ and $\mathring{a}_{\mathrm{in}}(355, 1064)$ data points referring to 5 September and 3 October 2011, respectively.

3 km a.g.l. Advection patterns similar to the one of Fig. 12a are rather frequent over south-eastern Italy, as mentioned in Sect. 4.2 (Perrone et al., 2013). It was also shown that they were mainly responsible for the advection of fine-mode particles caused by anthropogenic pollution (e.g. Perrone et al., 2013; Lelieveld et al., 2002). AERONET sun photometer measurements support the results revealed by Fig. 9. Table 2 shows that $\mathring{a}_{440,870}$ reached a rather large value (1.83) on 3 October 2011, in good accordance within uncertainties with the $\mathring{a}_{355,1064}(z)$ values of Fig. 9. In addition, we observe from Table 2 that the columnar value of $\eta_A(500\,\mathrm{nm}) = 0.86$ is in satisfactory accordance with the $\eta(z)$ mean values that can be estimated from Fig. 9 (open triangles). The $\Delta\mathring{a}(z)$-$\mathring{a}_{355,1064}(z)$ scatter plot of Fig. 9 (open triangles) indicates that the contribution of coarse-mode particle within 1.0–1.5 km a.g.l. was larger than the one within 2.0–2.5 km a.g.l. To this end, it is worth noting in Fig. 12b that 1 km arrival-height air masses crossed north-western Africa at very low altitudes before reaching south-eastern Italy, and as a consequence they have likely picked up a small amount of desert dust particles.

## 5 Overall results and discussion

The proposed graphical method was applied to lidar measurements performed on 10 days of the year 2011 to further demonstrate the method's ability to estimate the dependence on altitude of the fine-mode aerosol contribution to the aerosol optical thickness and of the fine-mode aerosol radius. Lidar measurement days were selected in order to have AOTs driven by the main sources characterizing aerosol particles over south-eastern Italy (Perrone et al., 2013). As mentioned, aerosols from continental Europe, the Atlantic Ocean and the Mediterranean Sea, and the African deserts are frequently advected over south-eastern Italy and more generally all over the central Mediterranean, as the study cases presented in Sect. 4 have revealed. Mean lidar ratios and calculated AOTs at the lidar wavelengths are given in Table 2, in addition to column-integrated microphysical parameters retrieved from AERONET (Lecce University) sun

photometer measurements collocated in time and space with lidar measurements, in order to highlight the differences between column integrated and corresponding vertically resolved aerosol parameters. Table 2 reveals that the investigated measurements days were characterized by AOTs spanning the 0.26–0.67, 0.15–0.39, and 0.05–0.27 range at 355, 532, and 1064 nm, respectively. Mean lidar ratios retrieved from the implemented iterative procedure varied within the 31–83, 32–84, and 11–47 sr range at 355, 532, and 1064 nm, respectively. Lidar ratio values depend on the aerosol optical and microphysical properties and are commonly used to distinguish aerosol of different types or origins by means of lidar measurements. Coarse non-absorbing aerosols such as sea-salt particles are characterized by small lidar ratio values (e.g. Barnaba et al., 2004). Conversely, fine absorbing particles such as soot are characterized by large lidar ratio values (e.g. Barnaba et al., 2007). Thus, measurements days affected by different aerosol types or sources were selected in accordance with aerosol parameters reported in Table 2. Columnar aerosol parameters retrieved from AERONET sun photometer measurements collocated in space and time with lidar measurements (Table 2) support the last statement. In fact, the AOT(500 nm), $\eta_{\mathrm{A}}(500\,\mathrm{nm})$, $\mathring{a}_{440,870}$, and $\Delta\mathring{a} = \mathring{a}_{440,675} - \mathring{a}_{500,870}$ spanned the 0.16–0.42, 0.32–0.93, 0.42–1.83, and −0.11–0.12 ranges, respectively, during the investigated measurement days. Numerical results showing the dependence of lidar ratios of fine- and coarse-mode particles on the complex refractive index for particles of different shapes have recently been reported by Lopatin et al. (2013). Lidar ratios have been provided at 355, 532, and 1064 nm. Lopatin et al. (2013) have found (Fig. 10 of their paper) that the lidar ratio spectral dependence is quite affected by the complex refractive index, shape, and size of particles. As a consequence, the lidar ratio changes with the wavelength are quite dependent on particle type, as the results of this paper have revealed (Table 2). Lopatin et al. (2013) found that the 1064 nm lidar ratios are always smaller than the corresponding ones at 532 and 355 nm. More specifically, they found that the 1064 nm lidar ratio of fine-mode particles is on average more than three times smaller than the one at 355 nm and takes values smaller than 20 sr for absorbing particles with the real part of the particle refractive index $n \geq 1.5$. Note that we have found (Table 2) relatively small and large lidar ratios at 1064 and 355 nm, respectively when fine-mode particles were dominant ($\eta_A \geq 0.84$), in satisfactory accordance with the results by Lopatin et al. (2013). More specifically, fine-mode particles were dominant on 28 July 2011 ($\eta_{\mathrm{A}} = 0.92$; Table 2), and we found a lidar ratio of $(11 \pm 10)$ sr and $(50 \pm 10)$ sr at 1064 and 355 nm, respectively. Lopatin et al. (2013) have also found that weakly absorbing coarse-spheroid particles with $n = 1.55$ are characterized by small lidar ratios (< 50 sr) at 355, 532, and 1064 nm, respectively. Table 2 shows that the contribution of coarse-mode particles was significant on 11 April 2011 ($\eta_{\mathrm{A}} = 0.32$) and it is interesting to observe that the retrieved lidar ratios at 1064 and 355 nm are equal to $(20 \pm 16)$ sr and $(40 \pm 4)$ sr, respectively, in satisfactory accordance with the results by Lopatin et al. (2013).

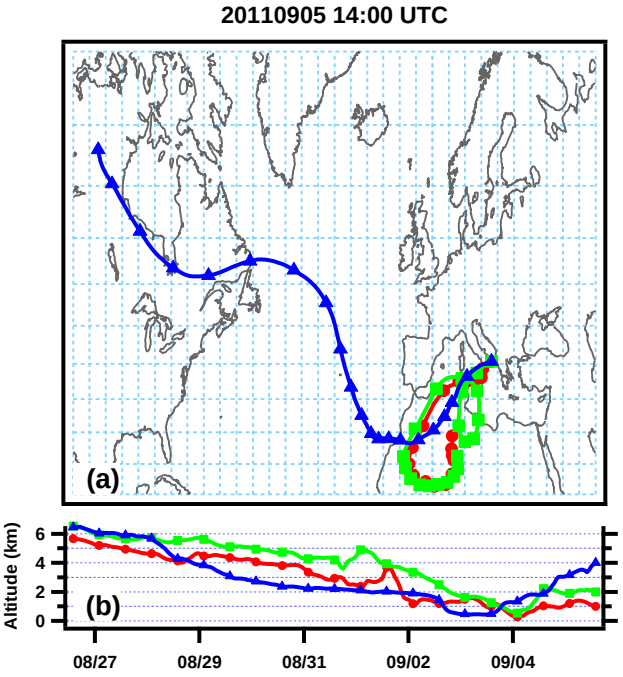


**Fig. 10. (a)** Pathways estimated for 14:00 UTC of 5 September 2011 of the ten day HYSPLIT back trajectories with arrival heights at 1, 2, and 4 km a.g.l. **(b)** Time evolution of the altitude of each back trajectory.

Figure 13 shows the scatter plot of LRs at 355 nm (dots), 532 nm (triangles), and 1064 nm (boxes) vs. the AOTs, at 355, 532, and 1064 nm, respectively. It is interesting to note that LR values that depend on aerosol optical and microphysical properties are weakly correlated to corresponding AOTs, as has commonly been found. This result indicates that AOTs are mainly driven by the concentration of aerosols of different optical and microphysical properties. Aerosol products from AERONET sun photometer measurements lead to the same conclusion. Figure 14 shows $\eta_A(500\,\mathrm{nm})$ and $\mathring{a}_{440,870}$ vs. the AOT at 500 nm by dots and triangles, respectively. $\eta_A(500\,\mathrm{nm})$ and $\mathring{a}_{440,870}$ depend on the aerosol microphysical properties and it is interesting to note that they do not reveal any marked dependence on the AOT: fine-mode dominated aerosols ($\eta_A > 0.6$, $\mathring{a}_{440,870} > 1.4$) and coarse-mode dominated aerosols ($\eta_A < 0.6$, $\mathring{a}_{440,870} < 0.8$) were responsible for high and low AOTs during the measurement days.

Open dots and error bars in Fig. 15a show the scatter plot of $\Delta\mathring{a}(z)$ vs. $\mathring{a}_{355,1064}(z)$ with corresponding uncertainties retrieved from lidar measurements performed on 10 different measurement days (Table 2). Different colours have been used to represent different measurement days as indicated at the top of Fig. 15a. Figure 15b shows the scatter plot of $\Delta\mathring{a}(z)$ vs. $\mathring{a}_{355,1064}(z)$ mean values without corresponding

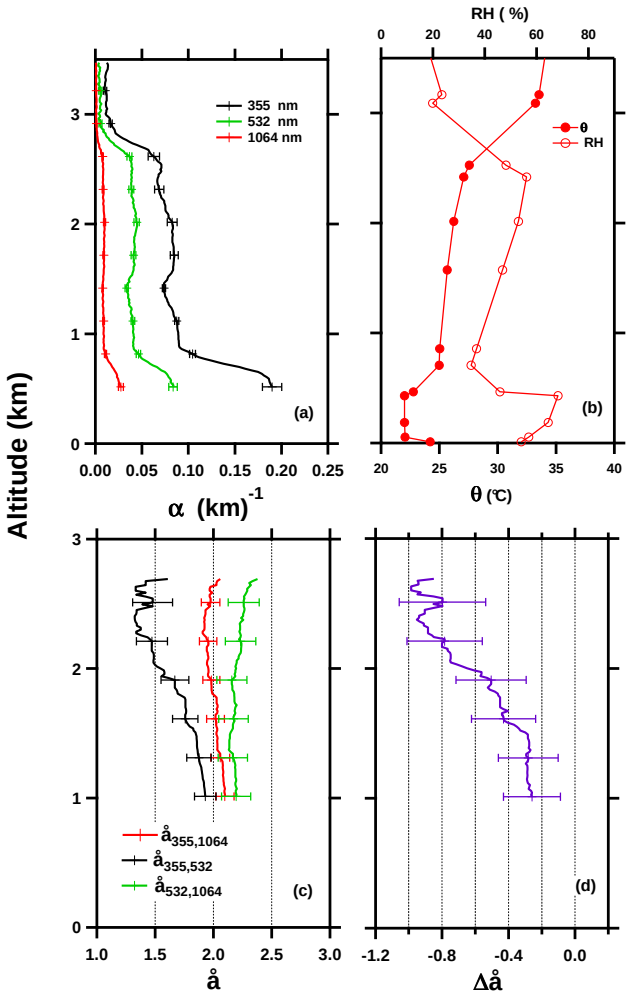


**Fig. 11. (a)** Extinction coefficient profiles at 355 nm (black line), 532 nm (green line), and 1064 nm (red line) retrieved from lidar measurements performed on 3 October 2011 from 12:41 to 13:16 UTC. **(b)** Vertical profiles of potential temperature ($\theta$) and relative humidity (RH) retrieved from radio sounding measurements performed at 11:00 UTC. Vertical profiles of **(c)** the Ångstrom exponents $\mathring{a}_{355,532}(z)$, $\mathring{a}_{532,1064}(z)$, $\mathring{a}_{355,1064}(z)$, and **(d)** the spectral curvature $\Delta\mathring{a}(z)$.

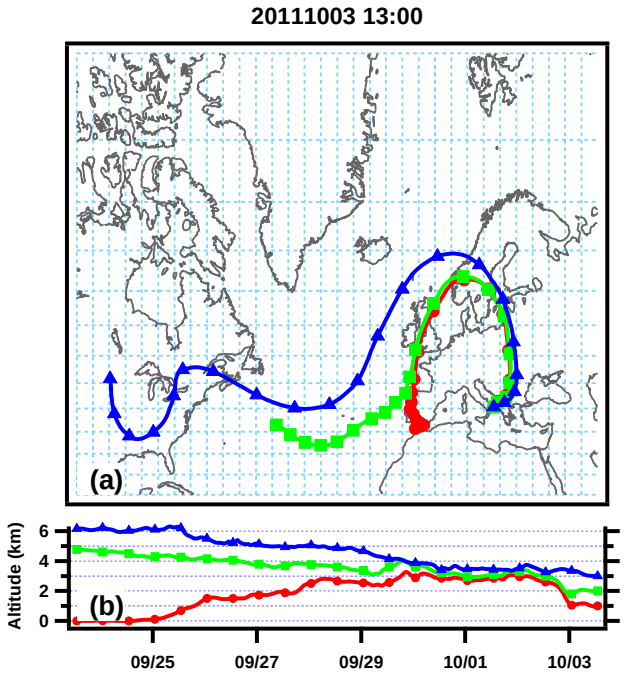


**Fig. 12. (a)** Pathways estimated for 13:00 UTC on 3 October 2011 of the ten day HYSPLIT back trajectories with arrival heights at 1, 2, and 4 km a.g.l. **(b)** Time evolution of the altitude of each back trajectory.

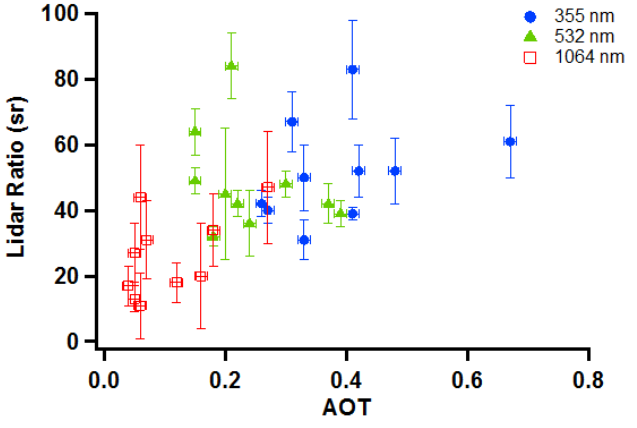


**Fig. 13.** Scatter plot of LRs at 355 nm (dots), 532 nm (triangles), and 1064 nm (boxes) vs. the AOTs at 355 nm, 532 nm, and 1064 nm, respectively.

uncertainties to better show how they vary with the monitoring day. $\mathring{a}(z)$ and $\Delta\mathring{a}(z)$ mean values span the 0.1–2.5 and −0.1–1.0 range, respectively, as a consequence of the high variability of the aerosol properties (Fig. 15b). Figure 16a shows the $\mathring{a}_{355,1064}(z)$ frequency of occurrence plot which is characterized by a bimodal distribution that peaks at about 0.3 and 1.6. The 0.3 peak value is likely due to the contribution of coarse-mode particles from the African deserts and/or the Atlantic Ocean and the Mediterranean Sea, as previous studies have indicated (Barnaba et al., 2004; Perrone et al., 2005; Perrone and Bergamo, 2011). The $\Delta\mathring{a}(z)$ frequency of occurrence plot (Fig. 16b) that peaks at about −0.3, is rather broad, with the mean value equal to 0.25 and the standard deviation equal to ±0.43. $\mathring{a}_{355,1064}(z)$ −$\Delta\mathring{a}(z)$ mean values lie within the graphical framework area delimited by $\eta(z)$ and $R_f$ $(z)$ values spanning the 0.30–0.99 and 0.05–0.30 µm range, respectively. The $\eta(z)$ variability range reveals that the aerosol particle size distribution is mainly bimodal. The spread of the $\mathring{a}_{355,1064}(z)$ −$\Delta\mathring{a}(z)$ data points allows for the identification of two main clusters. One cluster represents 40 % of the data points and it is associated with $\eta$ and $R_f$

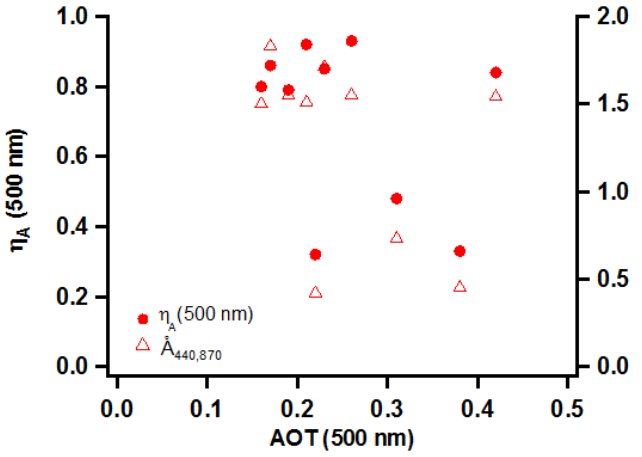


**Fig. 14.** Scatter plot of $\eta_A(500\,\text{nm})$ (dots) and $\mathring{a}_{440,870}$ (triangles) vs. the AOT(500 nm) retrieved from AERONET sun photometer measurements collocated in space and time with lidar measurements.

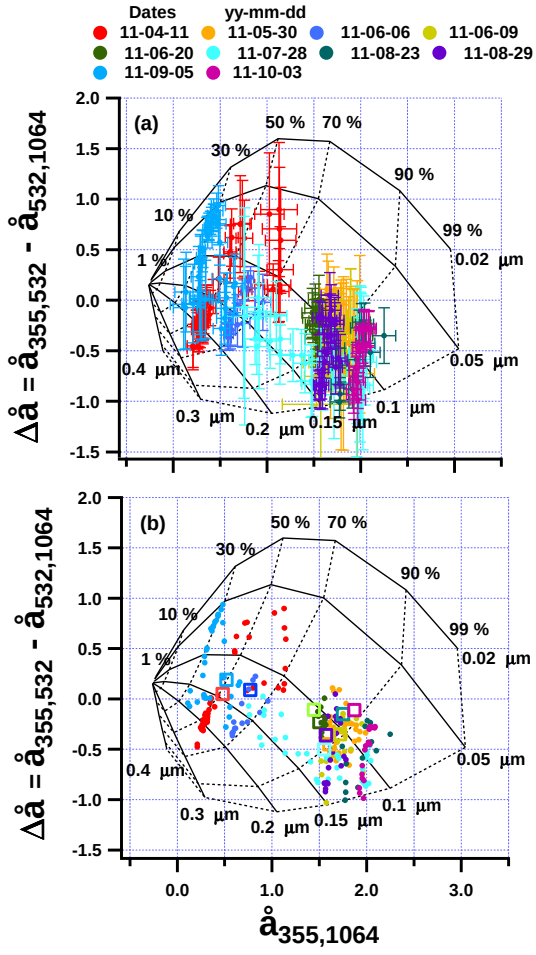


**Fig. 15. (a)** Scatter plot of $\Delta\mathring{a}(z)$ vs. $\mathring{a}_{355,1064}(z)$ with corresponding uncertainties retrieved from the lidar measurements performed on ten measurement days (Table 2). Different colours are used to represent different measurement days. **(b)** Scatter plot of $\Delta\mathring{a}(z)$ vs. $\mathring{a}_{355,1064}(z)$ mean values without corresponding uncertainties. The open boxes represent the $\Delta\mathring{a}_{\text{in}}$ and $\mathring{a}_{\text{in}}(355, 1064)$ data point for each measurement day.

values varying within the 30–70 % and 0.05–0.30 µm range, respectively. Four of the 10 measurement days contributed to this cluster where the contribution of coarse-mode particles increases as $\eta$ decreases. 60 % of the data points lie in the cluster delimited by the $\eta$ curves equal to about 80 and 99 %, respectively and the $R_f$ curves equal to about 0.05 and 0.15 µm, respectively (Fig. 15b). Fine-mode particles are dominant in this last cluster, and the high percentage of data points indicates that the contribution of fine-mode particles prevailed at the monitoring site of this study. Data points from seven measurement days contributed to this cluster. This last result indicates that the contribution of fine-mode particles was significant during almost all measurement days. These last results are supported by several studies performed by some of the authors of this paper (e.g. De Tomasi et al., 2006; Tafuro et al., 2007; Santese et al., 2008; Perrone et al., 2013) which revealed that the aerosol load over south-eastern Italy is significantly affected by fine pollution aerosols also due to long-range transported contributions from the surrounding populated regions. In particular, the analysis of more than one year of AERONET sun photometer measurements revealed that the aerosol volume size distribution was bimodal and that the volume (and mass) of aerosols smaller than 1 µm in maximum dimension (fine mode) was dominant during the entire year, and particularly during spring and summer (Tafuro et al., 2007). However, the bimodal structure of the dimensional spectrum reported in Tafuro et al. (2007) indicated that along with fine-mode particles, which were mainly of anthropogenic origin, coarse-mode particles, like the ones of natural (marine and crustal) origin, also contributed to the aerosol load during the entire year. Note that the results revealed by Fig. 15 are in satisfactory agreement with those reported by Basart et al. (2009) which depicted the dominance of fine-mode aerosols in driving the AOT at the monitoring site of this study. Quality-assured direct-sun observations of the Lecce University AERONET station, which included 2003–2007 annual cycles, were analysed by Basart et al. (2009).

Figure 15 shows that the increase of $\mathring{a}_{355,1064}(z)$ along constant $\eta$ curves is associated with the decrease of $R_f$. By contrast, the decrease of $\mathring{a}_{355,1064}(z)$ along constant $R_f$ curves is associated with the decrease of $\eta$ and hence, to the larger contribution of coarse-mode particles. 5 September and 3 October 2011 have been the days most affected by the contribution of coarse- and fine-mode particles, respectively (Fig. 9), as outlined in Sect. 4. Open boxes in Fig. 15b show $\Delta\mathring{a}_{\text{in}}$ vs. $\mathring{a}_{\text{in}}$ values calculated from the AOTs at 355, 532, and 1064 nm (Eqs. 4 and 5) to highlight the differences between columnar and vertically resolved $\mathring{a}_{355,1064}$ and $\Delta\mathring{a}$

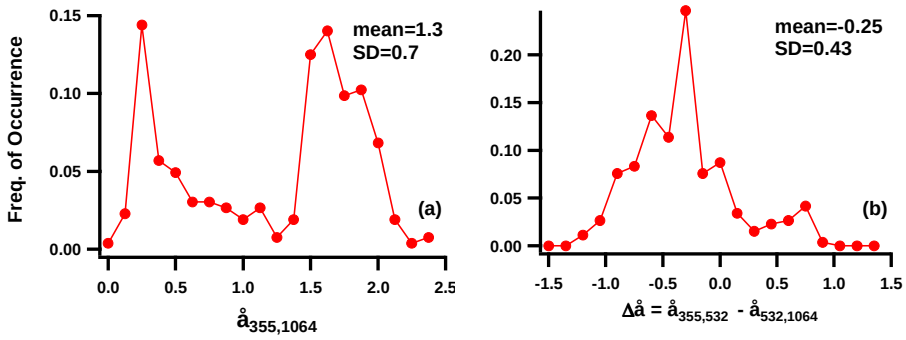


**Fig. 16.** Frequency of occurrence plot of **(a)** $\mathring{a}_{355,1064}(z)$ and **(b)** $\Delta\mathring{a}(z)$.

values for each of the analysed study cases. Figure 17 shows the scatter plot of $\Delta\mathring{a}(z)$ vs. $\mathring{a}_{355,1064}(z)$ mean values, using different colours to represent data referring to different altitudes a.g.l., in accordance with the colour bar on the top of the figure. It is interesting to note that Fig. 17 does not reveal any significant dependence of $\eta(z)$ and $R_f(z)$ on the altitude, at least for the analysed measurement days. In fact, the study-case analysis has clearly revealed that fine particles due to anthropogenic pollution and coarse particles of natural or anthropogenic origin could be found at any altitude sounded by the lidar. Data points retrieved from 1 up to ∼ 5 km a.g.l. contributed to the cluster delimited by the 80–90 % $\eta$ curves and the 0.05–0.15 µm $R_f$ curves, where fine-mode particles were prevailing, and to the cluster delimited by the 30–70 % $\eta$-curves and the 0.05–0.30 µm $R_f$-curves, where the contribution of coarse-mode particles was largest. The advection over south-eastern Italy of aerosol from continental Europe, the Atlantic Ocean and the Mediterranean Sea, and northern Africa contributed to these results, as previously mentioned.

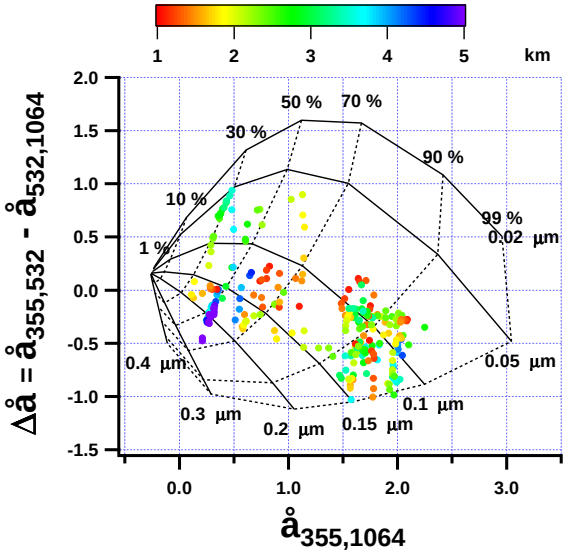


**Fig. 17.** Scatter plot of $\Delta\mathring{a}(z)$ vs. $\mathring{a}_{355,1064}(z)$ retrieved from the lidar measurements performed during 10 measurement days. Different colours are used to represent different altitudes a.g.l.

## 6 Summary and conclusion

The graphical method of Gobbi and co-authors has for the first time been used to track the changes with altitude of different aerosol types from 3-wavelength lidar profiles. The method relies on the use of a graphical framework and on the combined analysis of the Ångstrom exponent $\mathring{a}_{355,1064}(z)$ and its spectral curvature $\Delta\mathring{a}(z) = \mathring{a}_{355,532}(z) - \mathring{a}_{532,1064}(z)$, which were calculated from the lidar extinction profiles at 355, 532, and 1064 nm, respectively. Plotting data in the $\Delta\mathring{a}(z)$ vs. $\mathring{a}_{355,1064}(z)$ coordinates of the graphical framework allows one to obtain an estimate of the aerosol fine-mode radius $R_f(z)$ and fine-mode fraction $\eta(z)$ at different altitudes $z$. Lidar measurements performed on several days of the year 2011 were analysed to demonstrate the method feasibility. The measurement days were selected in order to have AOTs driven by the main sources of aerosol particles over south-eastern Italy. Aerosols from continental Europe, the Atlantic and Mediterranean Sea, and the African deserts are frequently advected over south-eastern Italy and more generally all over the central Mediterranean. As a consequence, aerosol types and hence, $R_f(z)$ and $\eta(z)$ may significantly vary with the altitude over south-eastern Italy. Linear particle depolarization ratio profiles from lidar measurements, AERONET (Lecce University) sun photometer measurements collocated in space and time with lidar measurements, MODIS satellite images, HYSPLIT analytical back trajectories, and the BSC–DREAM model were used to understand and support the dependence of $R_f$ and $\eta$ values retrieved from the proposed graphical method on $z$.

This paper's results have demonstrated the following:

a. $\eta(z)$ and $R_f(z)$ mean values varied within the 0.30–0.99 and 0.05–0.30 µm range, respectively and that

b. $R_f(z)$ and $\eta(z)$ varied significantly with altitude, mainly when aerosol of different types and hence from different sources were at different altitudes a.g.l.

c. It was found that $R_f(z)$ and $\eta(z)$ mean values were not dependent on the altitude from the ground level: fine particles due to anthropogenic pollution and coarse particles of natural or anthropogenic origin could be found at any altitude sounded by the lidar.

d. Results depicted the dominance of fine-mode aerosols in driving the AOT over south-eastern Italy: 60 % of the $R_f(z)$ and $\eta(z)$ mean values were within the 0.04–0.15 µm and 0.80-0.99 range, respectively. However, the $\eta(z)$ variability which spanned the 0.30–0.99 range has indicated that along with fine-mode particles, coarse-mode particles, which are of natural (marine and crustal) origin, also contributed to the aerosol load.

In conclusion, the results of this study have shown the feasibility of the proposed graphical approach to obtain an estimate of $R_f(z)$ and $\eta(z)$ from three-wavelength lidar measurements. The high variability of $R_f$ and $\eta$ with z has demonstrated the importance of accounting for the dependence of the aerosol microphysical properties on $z$. Several techniques have been developed in recent years to characterize the changes with altitude of the aerosol optical and microphysical properties from multi-wavelength lidar measurements, as it has been highlighted in the introduction. Each technique has its benefits and drawbacks and one must be aware that the uncertainties of retrieved aerosol parameters on average increase if the number of input parameters and hence, the number of optical channels in lidar systems decreases. However, it can be highly desirable/necessary to reduce the number of optical channels in some lidar experiments in order to obtain a lidar system more easy to handle. In fact, the three-channel lidar systems based on frequency tripled Nd-YAG laser are more widely spread throughout the world than Raman and high-spectral-resolution lidars. Therefore, the approach suggested in this study can be of interest mainly to users of three-channel lidar systems. We believe that the results on $R_f(z)$ and $\eta(z)$ combined with the column-integrated size distributions retrieved from AERONET sun photometer measurements collocated in space and time with lidar measurements, should allow obtaining particle size distributions dependent on $z$ by a closure analysis. Work in this direction is in progress. Finally, it is worth noting that the monitoring site of this study is on a flat peninsula of south-eastern Italy, more than 40 km away from large industrial sites. As a consequence, it can be considered representative of the aerosol load affecting the central Mediterranean. Hence, this paper's results have also highlighted some of the main features of the aerosol particles affecting the central Mediterranean and have revealed the importance of accounting for altitude-dependent size distributions in radiative transfer simulations.

*Acknowledgements.* This study was supported by the European Community through the ACTRIS Research Infrastructure Action under the 7th Framework Programme under ACTRIS Grant Agreement no. 262254. The authors would also like to acknowledge NASA/Goddard Space Flight Center and the Barcelona Super-Computing Centre for their contribution of satellite images and DREAM dust profiles, respectively. The authors gratefully acknowledge the NOAA Air Resources Laboratory (ARL) for the provision of the HYSPLIT back trajectories used in this publication. The authors gratefully acknowledge O. Cavalieri for carrying out some measurements and contributing to some data analyses.

Edited by: G. Feingold

## References

Ansmann, A., Seifert, P., Tesche, M., and Wandinger, U.: Profiling of fine and coarse particle mass: case studies of Saharan dust and Eyjafjallajökull/Grimsvötn volcanic plumes, Atmos. Chem. Phys., 12, 9399–9415, doi:10.5194/acp-12-9399-2012, 2012.

Barnaba, F., De Tomasi, F., Gobbi, G. P., Perrone, M. R., and Tafuro, A.: Extinction versus backscatter relationships for lidar applications at 351 nm: maritime and desert aerosol simulations and comparison with observations, Atmos. Res., 70, 229–259, 2004.

Barnaba, F., Tafuro, A. M., De Tomasi, F., and Perrone, M. R.: Observed and simulated vertically resolved optical properties of continental aerosols over southeastern Italy: A closure study, J. Geophys. Res., 112, D10203, doi:10.1029/2006JD007926, 2007.

Basart, S., Pérez, C., Cuevas, E., Baldasano, J. M., and Gobbi, G. P.: Aerosol characterization in Northern Africa, Northeastern Atlantic, Mediterranean Basin and Middle East from direct-sun AERONET observations, Atmos. Chem. Phys., 9, 8265–8282, doi:10.5194/acp-9-8265-2009, 2009.

Cavalieri, O., Perrone, M. R., De Tomasi, F., and Gobbi, G. P.: Three wavelengths lidar measurements for atmospheric aerosol characterization, Reviewed & Revised Papers of the 26th International Laser Radar Conference, 25–29 June, Porto Heli, Greece, Paper SO3-09, 2012.

Chaikovsky, A., Dubovik, O., Goloub, P., Tanre, D., Pappalardo, G.,Wandinger, U., Chaikovskaya, L., Denisov, S., Grudo, Y., Lopatsin, A., Karol, J., Lapyonok, T., Korol, M., Osipenko, F., Savitski, D., Slesar, A., Apituley, A., Alados Arboledas, L., Binietoglou, I., Kokkalis, P., Granados Munoz, M. J., Papayannis, A., Perrone, M. R., Pietruczuk, A., Pisani, G., Rocadenbosch, F., Sicard, M., De Tomasi, F., Wagner, J., and Wang, X.: Algorithm and software for the retrieval of vertical aerosol properties using combined lidar/radiometer data: dissemination in EARLINET, Reviewed & Revised Papers of the 26th International Laser Radar Conference, 25–29 June, Porto Heli, Greece, Paper SO3-09, 2012.

De Tomasi, F. and Perrone, M. R.: Lidar measurements of tropospheric water vapor and aerosol profiles over southeastern Italy, J. Geophys. Res., 108, 4286–4297, 2003.

De Tomasi, F. and Perrone, M. R.: PBL and dust layer seasonal evolution by lidar and radiosounding measurements over a peninsular site, Atmos. Res., 80, 86–103, 2006.

De Tomasi, F., Blanco, A., and Perrone, M. R.: Raman lidar monitoring of extinction and backscattering of African dust layers and dust characterization, Appl. Optics, 42, 1699–1709, 2003.

De Tomasi, F., Tafuro, A. M., and Perrone, M. R.: Height and seasonal dependence of aerosol optical properties over southeast Italy, J. Geophys. Res., 111, D10203, doi:10.1029/2005JD006779, 2006.

De Tomasi, F., Miglietta, M., and Perrone, M. R.: The Growth of the Planetary Boundary Layer at a Coastal Site: a Case Study, Bound.-Lay. Meteorol., 139, 521–541, doi:10.1007/s10546-011-9592-6, 2011.

Di Girolamo, P., Cacciani, M., Di Sarra, A., Fiocco, G., and Fuà, D.: lidar observations of the Pinatubo aerosol layer at Thule, Greenland, Geophys. Res. Lett., 21, 1295–1298, 1994.

Draxler, R. R. and Rolph, G. D.: HYSPLIT (HYbrid Single-Particle Lagrangian Integrated Trajectory) model, available at: http://www.arl.noaa.gov/ready/hysplit4.html (last access: May 20 2013), NOAA Air Resources Laboratory, Silver Spring, MD, 2003.

Dubovik O., Holben, B. N., Lapyonok, T., Sinyuk, A., Mishchenko, M. I., Yang, P., and Slutsker, I.: Non-spherical aerosol retrieval method employing light scattering by spheroids, Geophys. Res. Lett., 29, 1415, doi:10.1029/2001GL014506, 2002.

Fernald, F. G.: Analysis of atmospheric lidar observations: some comments, Appl. Optics, 23, 652–652, 1984.

Freudenthaler, V., Esselborn, M., Wiegner, M., Heese, B., Tesche, M., Ansmann, A., Muller, D., Althausen, D., Wirth, M., Fix, A., Ehret, G., Knippertz, P., Toledano, C., Gasteiger, G., Garhammer, M., and Seefeldner, M.: Depolarization ratio profiling at several wavelengths in pure Sahara dust during SAMUN 2006, Tellus B, 61, 165–179, 2008.

Gobbi, G. P., Kaufman, Y. J., Koren, I., and Eck, T. F.: Classification of aerosol properties derived from AERONET direct sun data, Atmos. Chem. Phys., 7, 453–458, doi:10.5194/acp-7-453-2007, 2007.

Gross, S., Tesche, M., Freudenthaler, V., Toledano, C., Wiegner, M., Ansmann, A., Althausen, D., and Seefeldner, M.: Characterization of Sahara dust, marine aerosols and mixtures of biomass-burning aerosols and dust by means of multi-wavelength depolarization and Raman lidar Measurements during SAMUN 2, Tellus B, 63, 706–724, 2011.

Holben, B. N., Eck, T. F., Slutsker, I., Tanré, D., Buis, J. P., Setzer, A., Vermote, E., Reagan, J. A., Kaufman, Y. J., Nakajima, T., Lavenu, F., Jankowiak, I., and Smirnov, A.: AERONET – A federate instrument network and data archive for aerosol characterization, Remote Sens. Environ, 66, 1–16, 1998.

Kaufman, Y. J.: Aerosol optical thickness and atmospheric path radiance, J. Geophys. Res., 98, 2677–2692, 1993.

Klett, J. D.: Lidar inversion with variable backscatter/extinction ratios, Appl. Optics, 24, 1638–1643, 1985.

Kolgotin, A. and Muller, D.: Theory of inversion with two-dimensional regularization: profiles of microphysical particle properties derived from multiwavelength lidar measurements, Appl. Optics, 47, 4472–4490, 2008.

Lelieveld, J., Berresheim, H., Bormann, S., Crutzen, P. J., Dentener, F. J., Fischer, H., Feichter, J., Flatau, P. J., Heland, J., Holzinger, R., Korrmann, R., Lawrence, M. G., Levin, Z., Markowicz, K. M., Mihalopoulos, N., Minikin, A., Ramanathan, V., de Reus, M., Roelofs, G. J., Scheeren, H. A., Sciare, J., Schlager, H., Schultz, M., Siegmund, P., Steil, B., Stephanou, E. G., Stier, P., Traub, M., Warneke, C., Williams, J., and Ziereis, H.: Global air pollution crossroads over the Mediterranean, Science, 298, 794–799, 2002.

Lopatin, A., Dubovik, O., Chaikovsky, A., Goloub, P., Lapyonok, T., Tanré, D., and Litvinov, P.: Enhancement of aerosol characterization using synergy of lidar and sun-photometer coincident observations: the GARRLiC algorithm, Atmos. Meas. Tech., 6, 2065–2088, doi:10.5194/amt-6-2065-2013, 2013.

Marenco, F., Santacesaria, V., Bais, A. F., Balis, D., Di Sarra, A., Papayannis A., and Zerefos, C.: Optical properties of tropodpheric aerosols determined by lidar and spectrophotometric measurements (Photochemical Activity and Solar Ultraviolet Radiation campaign), Appl. Optics, 36, 6875–6886, 1997.

Matthias, V., Freudenthaler, V., Amodeo, A., Balis, D., Boesenberg, J., Chaikovsky, A., Chourdakis, G., Comeron, A., Delaval, A., De Tomasi, F., Eixmann, R., Hagard, A., Komguem, L. , Kreipl, S., Matthey, R., Rizi, V., Rodrigues, J. A., Wandinger, U., and Wang, X.: Aerosol lidar intercomparison in the framework of the EARLINET project: 1. Instrument, Appl. Optics, 43, 961–976, 2004.

Muller, D., Ansmann, A., Mattis, I., Tesche, M., Wandinger, U., Althausen, D., and Pisani, G.: Aerosol-type-dependent lidar ratios observed with Raman lidar, J. Geophys. Res., 112, D16202, doi:10.1029/2006JD008292, 2007.

O'Neill, N. T., Eck, T. F., Smirnov, A., Holben, B. N., and Thulasiraman, S.: Spectral discrimination of coarse and ?ne mode optical depth, J. Geophys. Res., 108, 4559, doi:10.1029/2002JD002975, 2003.

Pahlow, M., Muller, D., Tesche, M., Eichler, H., Feingold, G., Eberhard, W., L., and Cheng, Y.: Retrieval of aerosol properties from combined multiwavelength lidar and sunphotometer measurements, Appl. Optics, 45, 7429–7442, 2006.

Perrone, M. R., Santese, M., Tafuro, A. M., Holben, B., and Smirnov, A.: Aerosol load characterization over South-East Italy for one year of AERONET sun-photometer measurements, Atmos. Res., 75, 111–133, 2005.

Perrone, M. R. and Bergamo, A.: Direct radiative forcing during Sahara dust intrusions at a site in the Central Mediterranean: Anthropogenic particle contribution. Atmos. Res., 101, 783–798, 2011.

Perrone, M. R., Tafuro, A. M., and Kinne, S.: Dust layer effects on the atmospheric radiative budget and heating rate profiles, Atmos. Environ., 59, 344–354, 2012.

Perrone, M. R., Becagli, S., Orza, J. A. G., Vecchi, R., Dinoi, A., Udisti, R., and Cabello, M.: The impact of long-range-transport on $PM_1$ and $PM_{2.5}$ at a Central Mediterranean site, Atmos. Environ., 71, 176–186, 2013.

Santese, M., De Tomasi, F., and Perrone, M. R.: Advection patterns and aerosol optical and microphysical properties by AERONET over south-east Italy in the central Mediterranean, Atmos. Chem. Phys., 8, 1881–1896, doi:10.5194/acp-8-1881-2008, 2008.

Schuster, G. L., Dubovick, O., and Holben, B. N.: Angstrom exponent and bimodal aerosol size distributions, J. Geophys. Res., 111, D07207, doi:10.1029/2005JD006328, 2006.

Seinfeld, J. H. and Pandis, S. N.: Atmospheric Chemistry and Physics: From Air Pollution to Climate Change, J. Wiley & Sons, INC, 1998.

Tafuro, A. M., Kinne, S., De Tomasi, F., and Perrone, M. R.: Annual cycle of aerosol direct radiative effect over southeast

Italy and sensitivity studies, J. Geophys. Res., 112, D20202, doi:10.1029/2006JD008265, 2007.

Takamura, T., Sasano, Y., and Hayasaka, T.: Tropospheric aerosol optical properties derived from lidar, sun photometer, and optical particle counter measurements, Appl. Optics, 33, 7132–7140, 1994.

Veselovskii, I., Kolgotin, A., Griaznov, V., Muller, D., Wandinger, U., and Whiteman, D.: Inversion with regularization for the retrieval of tropospheric aerosol parameters from multi-wavelength lidar sounding, Appl. Optics, 41, 3685–3699, 2002.

Veselovskii, I., Dubovik, O., Kolgotin, A., Korenskiy, M., Whiteman, D. N., Allakhverdiev, K., and Huseyinoglu, F.: Linear estimation of particle bulk parameters from multi-wavelength lidar measurements, Atmos. Meas. Tech., 5, 1135–1145, doi:10.5194/amt-5-1135-2012, 2012.

Wagner, R., Ajtai, T., Kandler, K., Lieke, K., Linke, C., Müller, T., Schnaiter, M., and Vragel, M.: Complex refractive indices of Saharan dust samples at visible and near UV wavelengths: a laboratory study, Atmos. Chem. Phys., 12, 2491–2512, doi:10.5194/acp-12-2491-2012, 2012.